FY 2014 Status Report: Vibration Testing of High-Burnup Clad/Fuel

Fuel Cycle Research & Development

Prepared for
U.S. Department of Energy
Used Fuel Disposition Campaign
B. B. Bevard, R. L. Howard,
J. A. Wang, H. Wang, H. Jiang
Oak Ridge National Laboratory

March 28, 2014
FCRD-UFD-2014-000487

Oak Ridge National Laboratory is a multi-program laboratory managed and operated by UT-Battelle, LLC for the U.S. Department of Energy under contract DE-AC05-00OR22725.

SUMMARY

This report documents ongoing work performed at Oak Ridge National Laboratory (ORNL) for the Department of Energy, Office of Fuel Cycle Technology Used Fuel Disposition Campaign (UFDC), and satisfies the deliverable for milestone M4FT-14OR0805033, *Status Report of Vibration Testing of Clad Fuel*. This work is conducted under WBS 1.02.08.05, Work Package FT-14OR080503 "Experiments – ORNL."

The objectives of this work package are to:

(1) develop a UFD Experiments Test Plan that will support development of on-going program modeling efforts and provide information that may eventually be used to develop the technical bases:

- to support the continued safe and secure storage of UNF for extended periods;
- for retrieval of UNF after extended storage; and
- for transport of high burnup fuel, as well as low and high burnup fuel after dry storage.

The test plan includes finite element analysis (FEA) to inform the program concerning clad/fuel separate effects and combined effects, and hot-cell and out-of-hot-cell testing on irradiated and unirradiated cladding and clad/fuel clad/fuel samples;

(2) perform out-of-cell testing to inform follow-on in-cell testing; and

(3) conduct initial in-cell testing of UNF, as described in the Experiments Test Plan.

ORNL's FY 2014 activities include the following:

- Development of the UFD Experiments Test Plan
- Assembly of an out-of-cell vibration test machine (Cyclic Integrated Reverse Bending Fatigue Tester – CIRFT)
- Separate effects testing using the CIRFT and surrogate fuel
- Testing of UNF using the CIRFT in the ORNL hot cell

This page intentionally left blank.

CONTENTS

This page intentionally left blank.

FIGURES

TABLES

This page intentionally left blank.

ACRONYMS

CIRFT	cyclic integrated reversible-bending fatigue tester
EI	flexural rigidity
FEA	finite element analysis
HFIR	High Flux Isotope Reactor
LVDT	linear variable differential transformers
M	bending moments
NCT	normal conditions of transportation
NRC	US Nuclear Regulatory Commission
ONRL	Oak Ridge National Laboratory
PNNL	Pacific Northwest National Laboratory
UNF	used nuclear fuel
UFDC	used fuel disposition campaign

This page intentionally left blank.

USED FUEL DISPOSITION CAMPAIGN

FY 2014 STATUS REPORT: VIBRATION TESTING OF CLAD FUEL

1. UFD EXPERIMENTS TEST PLAN

1.1 Introduction

During normal reactor operations, the nuclear fuel in a reactor experiences corrosion, which results in the formation of a waterside corrosion layer (oxide) and the introduction of hydrogen into the zirconium (Zr) cladding via the reaction $2H_2O+Zr \rightarrow ZrO_2+4H$. With increasing corrosion, the hydrogen concentration in the cladding will exceed its terminal solid solubility and brittle zirconium hydrides ($Zr+2H \rightarrow ZrH_2$) may precipitate as the cladding cools. This causes cladding ductility and failure energy to decrease [1–3], weakening the cladding. This cladding degradation due to hydride precipitates increases the likelihood of cladding failure during very long-term storage and/or transportation of used nuclear fuel (UNF).

The DOE Used Fuel Disposition Campaign (UFDC) tasked Oak Ridge National Laboratory (ORNL) to investigate the behavior of light-water-reactor (LWR) fuel cladding material performance related to extended storage and transportation of UNF. ORNL has been tasked to perform a systematic study on UNF integrity under simulated normal conditions of transportation (NCT) by using the recently developed hot-cell testing equipment, Cyclic Integrated Reversible-Bending Fatigue Tester (CIRFT) [1–9], developed in support of a similar Nuclear Regulatory Commission (NRC) project.

To support and prioritize the testing, ORNL has developed the UFD Experiments Test Plan. This plan will help develop information to support ongoing program modeling efforts and will provide information that may be used to support licensing activities. The test plan includes finite element analysis (FEA) to inform the program concerning clad/fuel separate effects and combined effects, and hot-cell and out-of-hot-cell testing on irradiated and unirradiated cladding and clad/fuel samples.

The plan describes recommended tests to be done and a potential order of those tests. However, many of the tests will include elements of FEA, followed by out-of-cell testing and eventually in-cell testing, so that the actual test matrix will be developed based on the results of the previous activity.

An out-of-hot-cell CIRFT has been developed and will be used to support both proof of principle and out-of-hot-cell separate effects testing prior to tests on UNF in the hot cell. The out-of-cell tests will evaluate pellet/clad features such as clad/fuel bonding effects, fuel chamfer, clad creep down, effects of clad hydrogen level, and other clad/fuel mechanical properties to determine which properties should be investigated in the hot cell tests.

To support the testing on actual high-burnup UNF, fast-neutron irradiation of pre-hydrided zirconium-alloy cladding in the High Flux Isotope Reactor (HFIR) at elevated temperatures will be used to simulate the effects of high-burnup on fuel cladding for help in understanding the cladding materials properties relevant to extended storage and subsequent transportation. The irradiated pre-hydrided metallic materials testing will generate baseline data to benchmark hot-cell testing of the actual high-burnup UNF cladding. More importantly, the HFIR-irradiated samples will be free of alpha contamination and can be provided to researchers who do not have hot cell facilities to handle highly contaminated high-burnup UNF cladding to support their research projects for the UFDC.

In order to accomplish this research, ORNL will also utilize unirradiated cladding samples provided by Pacific Northwest National Laboratory (PNNL) that have been subjected to pre-hydride treatment. Additionally, ORNL will pre-hydride some unirradiated cladding samples to provide enough test samples to establish a relevant test sample base.

1.2 Test Plan Background Information

UNF that has been irradiated to high-burnup levels (> 45 GWd/MTU) and placed in dry storage casks (vacuum dried and heated to remove residual moisture) can exhibit a number of properties and conditions of interest to the UFD program (Table 1).

Table 1. Clad/fuel properties of interest to UFD Program

Property	Area of Interest	Need
What is the associated fracture toughness for both irradiated fuel pellets and clad. Fractured fuel pellets (due to irradiation & fission gas); fuel may have voids or chips due to manufacturing defects.	How much contribution to fuel rod strength does the fuel supply? How does fracturing affect this contribution?	Fuel contribution to rod strength
Significant pellet to clad bonding (bonding initiates during the first irradiation cycle – 23 MWd/MTU); however, the fuel may be circumferentially cracked near the clad due to uneven cool down of the dissimilar materials (clad and fuel). Modelers are assuming some effective gap.[a]	Can the bonding be measured and or quantified to support modeling. Is there a detectable difference when the fuel has more cracking?	Strength of clad/fuel bonding layers [b]
What is the associated interface fracture toughness or interface cohesion bond? Pellet-pellet bonding (will increase with burnup)	What is the contribution of the pellet-pellet bond to the rod strength under load?	The interface fracture toughness and interface de-bond threshold property indicates the allowable vibration intensity before rod failure.
Internal rod pressure – pressure will have increased from original fill gas pressure due to fission gas release during irradiation; the higher the burnup, the higher the internal gas pressure (in addition to irradiation-induced residual tensile stress in the clad).	How does the amount of internal gas pressure and the existing stress profile within clad structure affect hydride reorientation; does internal gas pressure affect the results of fueled cladding tests?	Accurate description of stress and load conditions in the irradiated fuel-clad system.
Clad cracks/pin holes – there may be clad failures that have released the fission gas and/or weakened the clad.	How do existing defects affect fuel rod integrity under NCT?	Fracture toughness of aging clad composite system, including oxide and hydride embrittlement effect evaluation.

Property	Area of Interest	Need
Hydride rim on the outer circumference of the cladding	How does the hydride rim affect rod system strength?	Fracture toughness of defueled clad
Circumferential hydriding throughout the cladding	What is the effect of the circumferential hydrides on the rod strength?	Understand how hydrides affect fuel strength for different cladding materials
Radial hydriding throughout the cladding due to the effects of internal rod pressure and heating during the drying process (the current assumption is that all circumferential hydrides reorient and become radial hydrides in the drying process)	Do all hydrides reorient during the drying cycle? How much do radial hydrides affect the rod strength during NCT?	Understanding of how hydrides affect fuel strength for different cladding materials; fracture toughness data are needed to quantify this phenomenon
Oxide layer on the outer clad surface (oxide layers will vary by clad material and irradiation history) – reduces clad thickness	How does reduced clad thickness affect rod strength during NCT	
Related issues include original clad thickness, including the clad/fuel volume ratio	How does reduced clad thickness affect rod strength during NCT; and the fuel clad volume ratio to the stiffness and vibration response of the fuel-clad system	

[a] *UNF Loading and Structural Performance Under NCT – Modeling Simulation and Experimental Integration RD&D Plan,* p. 30 (April 1, 2013).

[b] *UNF Loading and Structural Performance Under NCT – Supporting Material Properties and Modeling Inputs,* p. 55, p. 12 – Recrystallization (March 16, 2013).

This page intentionally left blank.

2. STATUS OF THE OUT-OF-CELL CYCLIC REVERSAL BENDING FATIGUE TESTER (CIRFT) FOR SPENT FUEL VIBRATION INTEGRITY TESTING

2.1 Background

Under current US NRC rules, it is not sufficient for UNF to simply maintain its integrity during the storage period. It must maintain its integrity in such a way that it can withstand the physical forces of handling and transportation associated with restaging the fuel and moving it to treatment or recycling facilities, or to a geologic repository or other storage facility. Hence it is necessary to understand the performance characteristics of aged UNF cladding and the UNF pellets it surrounds under loads stemming from handling and transport initiatives. For NCT, vibration loads incident to transport must be considered. As the burnup of the fuel increases, a number of changes occur that may affect the performance of the fuel and cladding in storage and during transportation. Spent fuel cladding has traditionally provided defense-in-depth as the primary fission product barrier in the nuclear fuel cycle, and has been relied upon to provide geometry control for criticality safety during transportation. The mechanical properties of high-burnup de-fueled cladding have been previously studied by subjecting defueled cladding tubes to longitudinal (axial) tensile tests, ring-stretch tests, ring-compression tests, and biaxial tube burst tests. The objective of the bend test is to investigate the mechanical properties and behavior of both the cladding and the fuel in the cladding (including inertia-induced fuel pellet and clad interaction) under vibration/cyclic loads similar to the sustained vibration loads experienced during NCT.

The vibration loads experienced by UNF rods during transportation can be characterized as dynamic, cyclic, bending loads. The transient vibration signals in a specified transport environment can be analyzed, and frequency, amplitude, and phase components of the vibration can be identified. The methodology developed at ORNL supports the study of the vibration integrity of actual UNF rod segments through the testing and evaluation of the fatigue performance of UNF rods at defined frequencies and loads. ORNL has developed a fatigue system to evaluate the response of the UNF rods to vibration loads, as noted in Refs.7, 8, 9 and 10. A three-point deflection measurement technique using linear variable differential transformers (LVDTs) is used to characterize the rod curvature of samples under test conditions, and electromagnetic force linear motors are used as the driving system to provide the mechanical load. ORNL has developed both an out-of-cell and an in-cell CIRFT to perform UNF vibration testing on both surrogate and high-burnup fuel to evaluate the effect of pellet-clad interactions and the effects of material bonding on the effective lifetime of the fuel-clad structure bending fatigue performance.

2.2 CIRFT Concept

The reverse pure bending is conducted using a U-frame testing setup. A conceptual U-frame setup is shown in Figure 1. The U-frame is constructed with two rigid arms and the associated linking members. The rod specimen is coupled with the U-frame by inserting the specimen into the co-linear holes in the two rigid arms. As a result, reverse bending is applied to the rod specimen when a controlled push-pull force is applied to the two loading points of the rigid arms. This test system is able to capture the pure reverse bending and is designed to allow testing in a hot cell (CIRFT can be operated using remote-handling manipulators). To facilitate use in the hot cell, the system has a minimum number of moving parts and test sample installation is achieved using a simple drop-in action. The test system is designed to use a 6 in. rod segment with a 2 in. gage section. The majority of the test system components are made of stainless steel (SS) 304. Prior to initial equipment design, 3-D FEA showed that the position of the rod

specimen relative to the linking members of the U-frame had a significant impact on the amount of stress applied to the test specimen. Using appropriate compliant layers in each grip allowed a pure bending moment to be achieved in the test specimen gage section, as shown in Figure 2. The maximum von Mises stress level occurred at the pellet-clad interface.

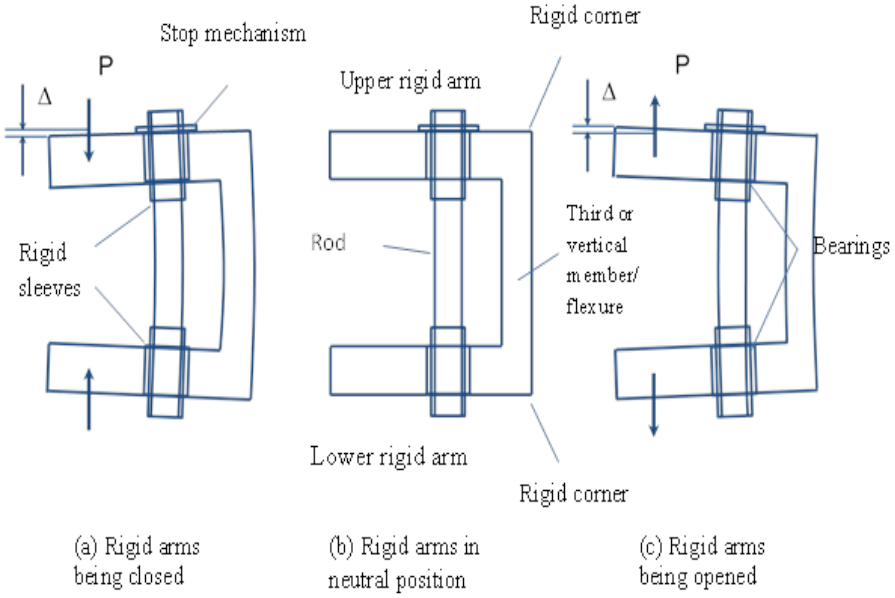

Figure 1. U-frame-assisted bending fatigue testing setup for reversal bending when rigid arms are (a) closing, (b) neutral, and (c) opening.

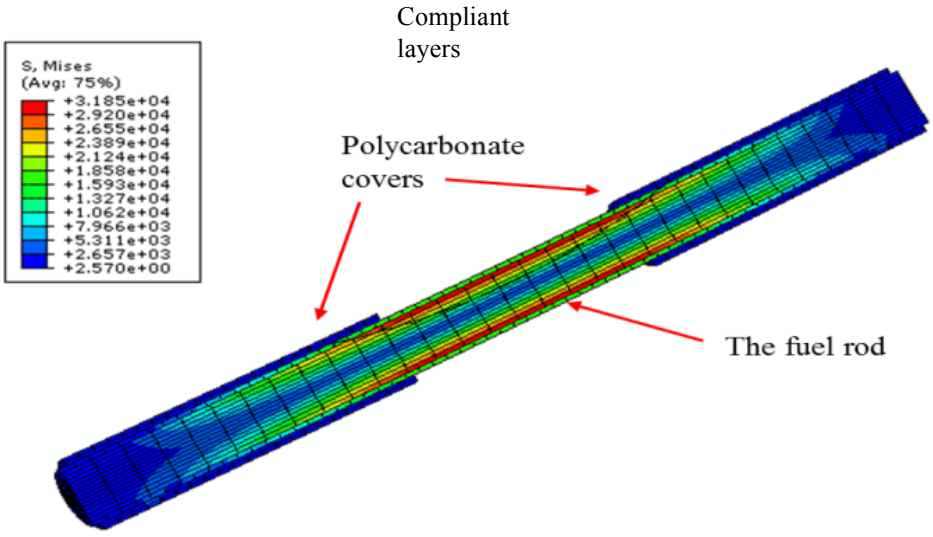

Figure 2. Stress distribution in a fuel rod with compliant layer when the applied force was 178 N; the unit of stress is psi. The maximum von Mises stress is 220 MPa (3.185×104 psi).

2.3 CIRFT Out-of Cell Equipment Status

The current configuration of the out-of-cell CIRFT apparatus has the U-frame set horizontally and uses a dual Bose linear motor test bench as shown in Figure 3.This alignment eliminates the effect of the U-frame self-weight entirely; also the push-pull force is applied symmetrically at both loading points by use of the dual linear motors. This design allows the use of a wide frequency range when applying pure bending to the test specimen during dynamic cycling. Moreover, the Bose linear motors use electromagnetic forces to generate the driving forces, and thus there are no oil issues affecting hot cell use as would occur when using a servo-hydraulic test machine.

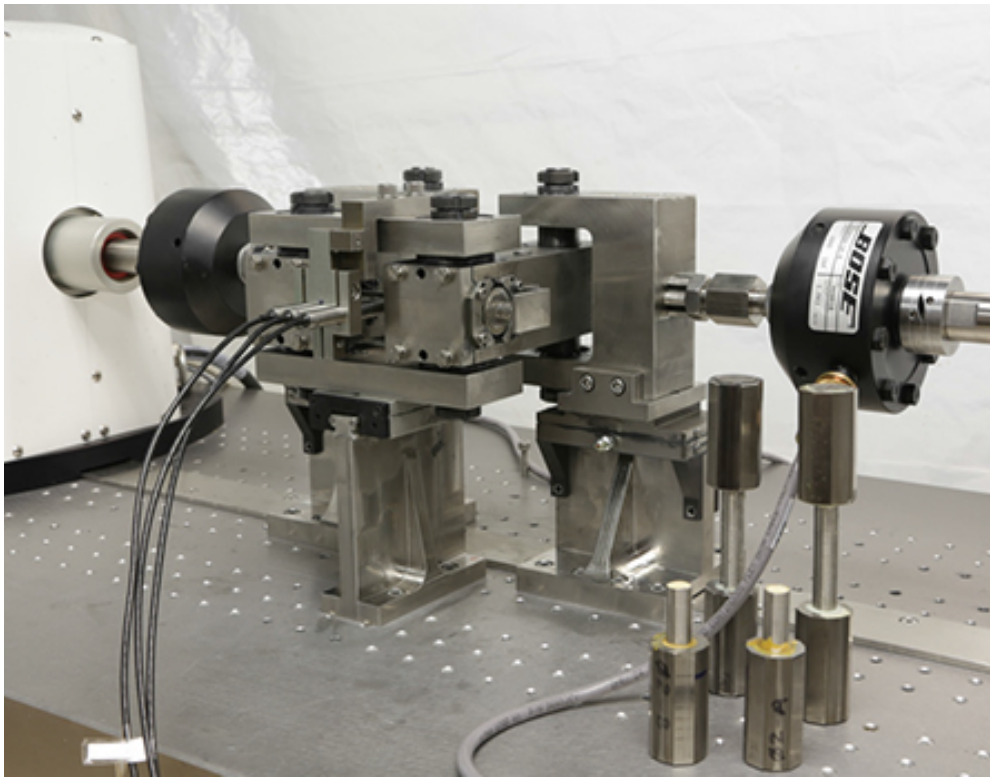

Figure 3. Integrated ORNL U-frame Bose dual linear motor test bench. A horizontal arrangement is used to eliminate the effect of the U-frame mass on the specimen.

2.4 CIRFT Hardware Description

The out-of-cell CIRFT was assembled in early December 2013. The system consists of dual LM2 Bose test bench and U-frame testing setup and is equipped with three LVDTs to measure test specimen deflections at three points for curvature measurement. Two 3000 N load cells and two 12.5 mm LVDTs are used in the Bose machines for control and measurement. The U-frame has a 101.60 mm loading arm, and the three curvature LVDTs have a ±5mm measurement range.

The overall setup, power modular, PCI-82 controller, three curvature LVDT amplifiers and power supplies are shown in Figure 4, Figure 5, and Figure 6. Three D6 (±2.5mm) LVDTs were used in the current testing setup. They were calibrated and integrated into Bose PCI-82. The calibration results are given in Figure 7 for one of the LVDTs.

The configuration of the out-of-cell CIRFT is identical to the one that was moved into the hot cell (ORNL Building 3525) at the end of September 2013 to conduct the bend tests sponsored by the NRC.

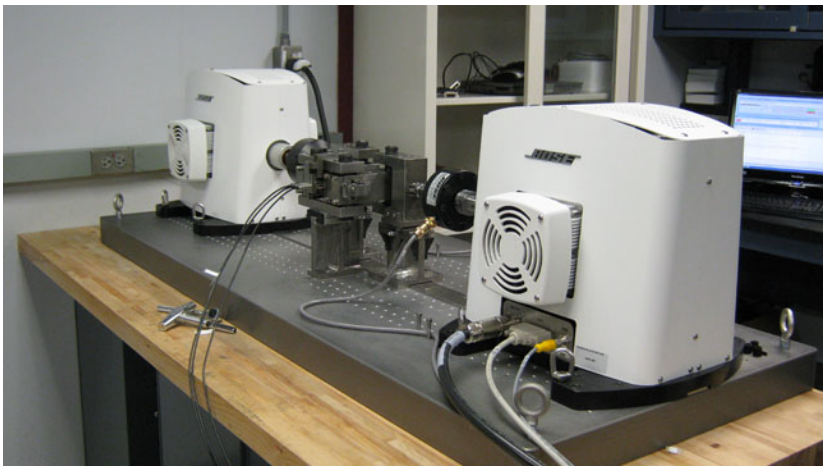

(a)

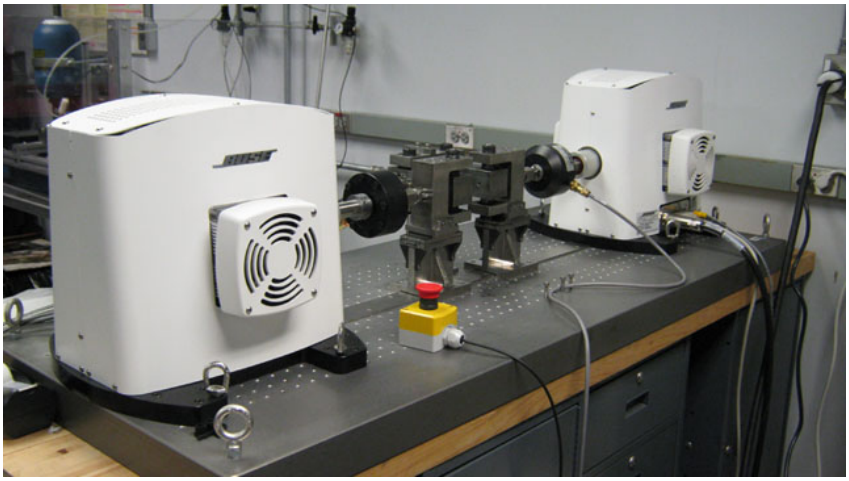

(b)

Figure 4. (a) Front and (b) back view of assembled U-frame to Bose dual LM2 Test Bench.

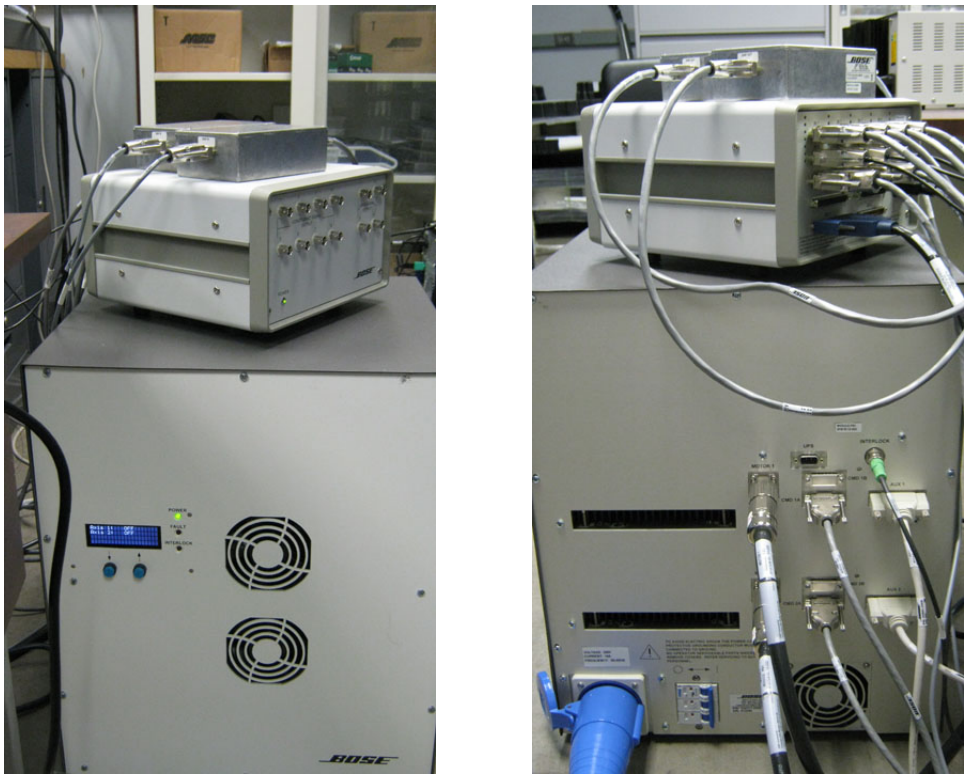

(a) (b)

Figure 5. (a) Front and (b) back view of power modular, PCI control, and LM2 LVDT amplifiers.

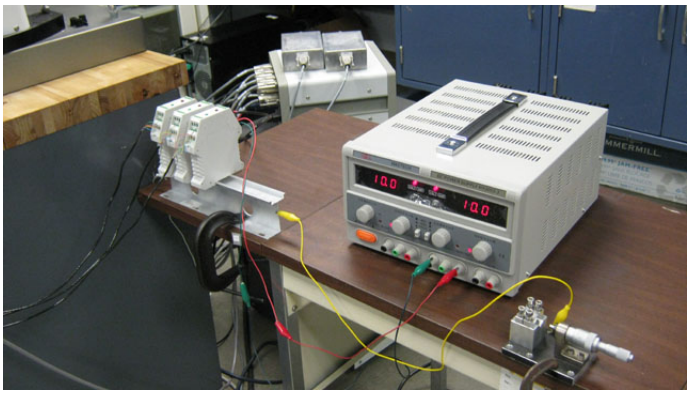

(a)

(b)

Figure 6. (a) Amplifier, power supply, calibration setup of three curvature LVDTs, and (b) the integrated channels of LM2 load cells, LM2 LVDTs, and three curvature LVDTs into Bose PCI controller.

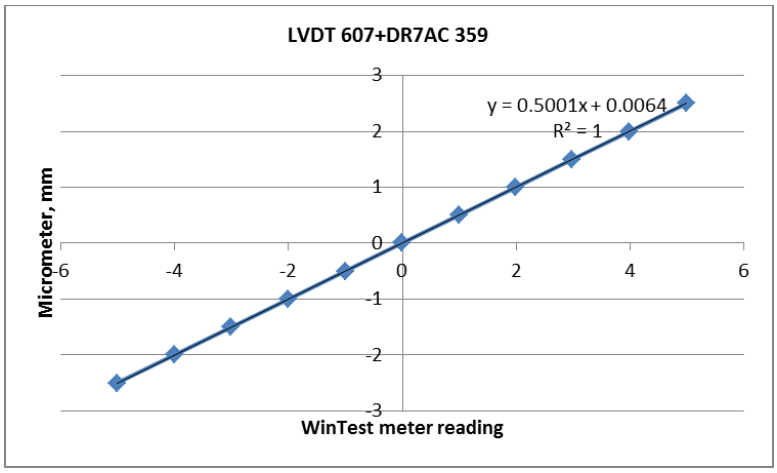

Figure 7. Calibration results of LVDT 607 with DR7AC 359.

2.5 Experimental Demonstration

The CIRFT proof-of-principle demonstrations including out-of-hot cell testing on Zircaloy-4 samples with and without bonded surrogate fuel pellets are described in detail in the report *FY 2013 Summary Report: Post-Irradiation Examination of Zircaloy-4 Samples in Target Capsules and Initiation of Bending Fatigue Testing for Used Nuclear Fuel Vibration Integrity Investigations*, Oak Ridge National Laboratory, September 30, 2013, FCRD-UFD-2013-000369 [14].

2.6 Probe Effect Study on Curvature Measurement

In order to improve the effectiveness of the CIRFT LVDT measurement system, the potential effect of the LVDT probe head size on the curvature measurement of a test specimen, especially when the test load amplitude is small, was examined. The contact of the probe on the bending test specimen may shift as the test specimen bending direction changes. This effect depends on the LVDT head contact diameter (h), as shown in Figure 8.

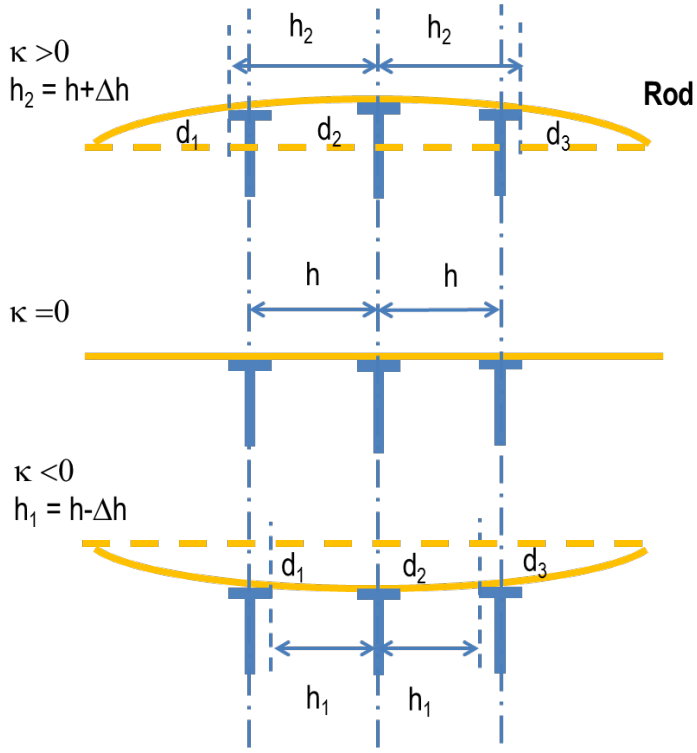

Figure 8. Diagram showing that the deflections measured by LVDTs may vary depending on contact with the test specimen.

The probe study was carried out on a test sample using LVDTs with both flat disk contact and chisel head contact (Figure 9). Small-amplitude low-frequency measurements were conducted where loads were controlled so that the irreversible deformation of the test specimen would be negligible and results could be compared. The tests under ±0.3 to 0.5 mm deflection showed that the difference in curvature responses of the test specimen measured by the two types of probes was relatively small; one test case is shown in

Figure 10Figure 10. Moment-curvature plots showed only a slightly left shift (~ 7.7%), as shown in Figure 10(b), when the chisel contact was used. This observation suggests that the correction for the probe head contact effect is not significant and is much less than that the correction factor predicted by the theoretical formulation, as illustrated in Figure 11. For example, substituting a contact diameter of 6 mm into the probe head model results in an ~ 22% increase in curvature range given 1.0 mm relative displacement input (Figure 11). Instead, the 7.7% maximum offset was observed in the chisel head contact test. Therefore, considering the dynamic noise and the probe head contact observation, the data generated using flat probes in the hot cell dynamic tests will be processed without any correction.

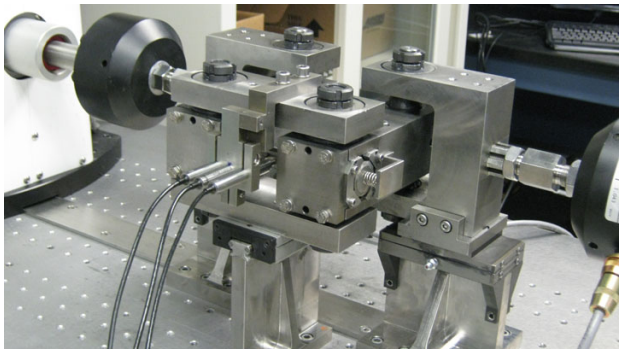

(a)

(b)

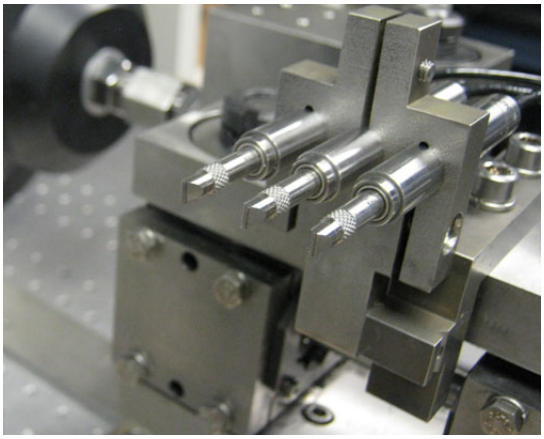

(c)

Figure 9. (a) Three curvature LVDTs were being held against the rod; (b) LVDT clamp was open to show (1) flat probe in one configuration and (2) chisel probe in another configuration.

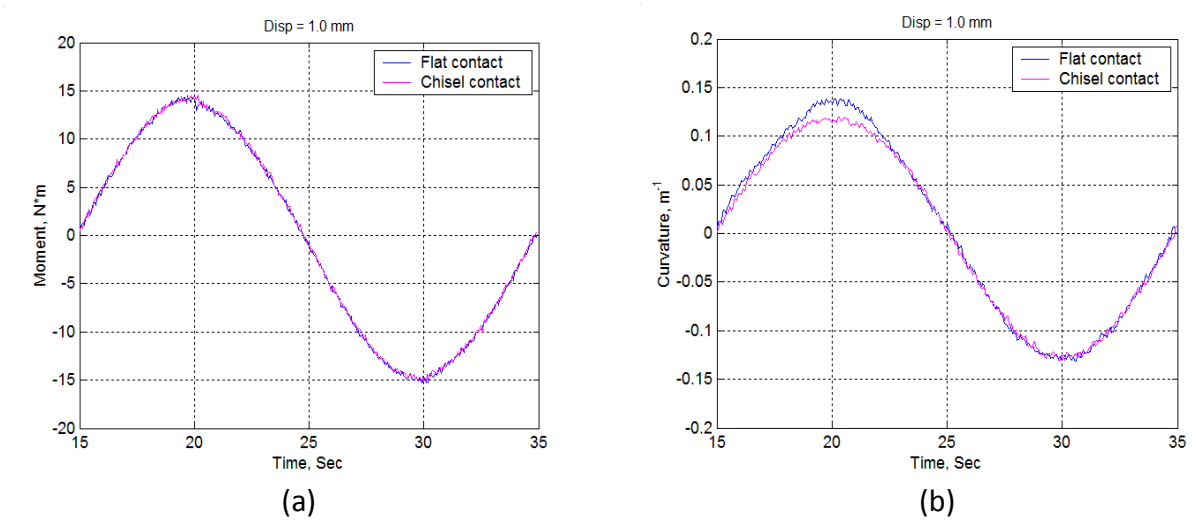

Figure 10. (a) Moment and (b) curvatures based on results with relative displacement 1.0 mm.

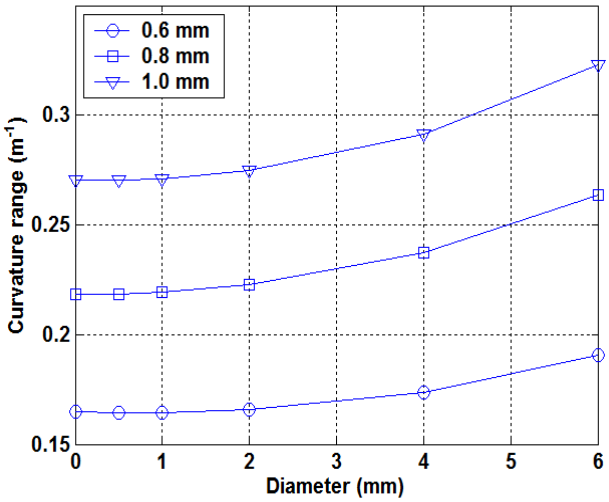

Figure 11. Curvature range corrected as a function of contact diameter under various relative displacements.

2.7 Test Protocol Development

Three test procedures were evaluated: 1) cycling without stop, 2) cycling with stop but no channel reset (i.e., no re-initialization of test conditions), 3) cycle with both stop and channel reset to initial test conditions. For this procedure development, a frequency of 5 Hz was used while the load amplitude was controlled at a low level to minimize rod deformation during testing (Table 2). Both chisel head and flat contacts were tested. Under the test conditions, no significant change in curvature response of the test specimen was noted between procedure 1 and 2 (Figure 12) or between procedure 1 and 3 (Figure 13) for either the chisel head contact or for the flat head contact. The positions where the tests were stopped and restarted are marked with red arrows.

Table 2. Three test procedures were evaluated: 1) cycle w/o stop, 2) cycle w/ stop but no channel reset, 3) cycle w/ stop and channel reset.

Date	No.	pk1 (mm, N)	pk2 (mm, N)	Freq (Hz)	Increment	Total cycles	Note
1/14/2014	1	-100	100	5	10000	10000	chisel, no stop
1/14/2014	2	-100	100	5	1000	1000	chisel, stop w/o reset
1/14/2014	3	-100	100	5	4000	5000	chisel, stop w/o reset
1/14/2014	4	-100	100	5	5000	10000	chisel, stop w/o reset
1/14/2014	5	-100	100	5	1000	1000	chisel, stop w/ reset
1/14/2014	6	-100	100	5	4000	5000	chisel, stop w/ reset
1/14/2014	7	-100	100	5	5000	10000	chisel, stop w/ reset
1/17/2014	41	-100	100	5	10000	10000	flat, no stop
1/17/2014	42	-100	100	5	1000	1000	flat, stop w/o reset
1/17/2014	43	-100	100	5	4000	5000	flat, stop w/o reset
1/17/2014	44	-100	100	5	5000	10000	flat, stop w/o reset
1/21/2014	45	-100	100	5	1000	1000	flat, stop w/ reset
1/21/2014	46	-100	100	5	4000	5000	flat, stop w/ reset
1/21/2014	47	-100	100	5	5000	10000	flat, stop w/ reset

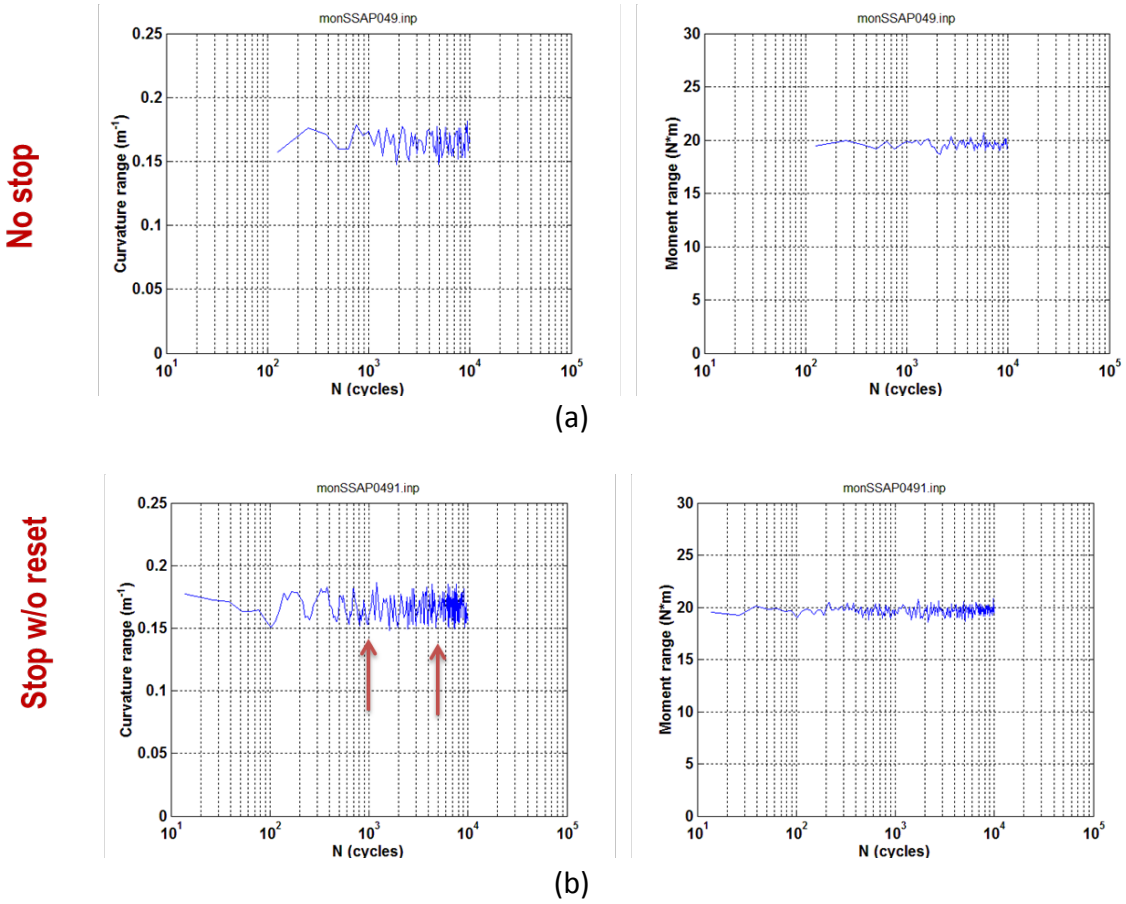

Figure 12. No significant changes in curvature response observed between (a) procedure 1 and (b) procedure 2 for chisel head contact. The red arrow indicates the stop location.

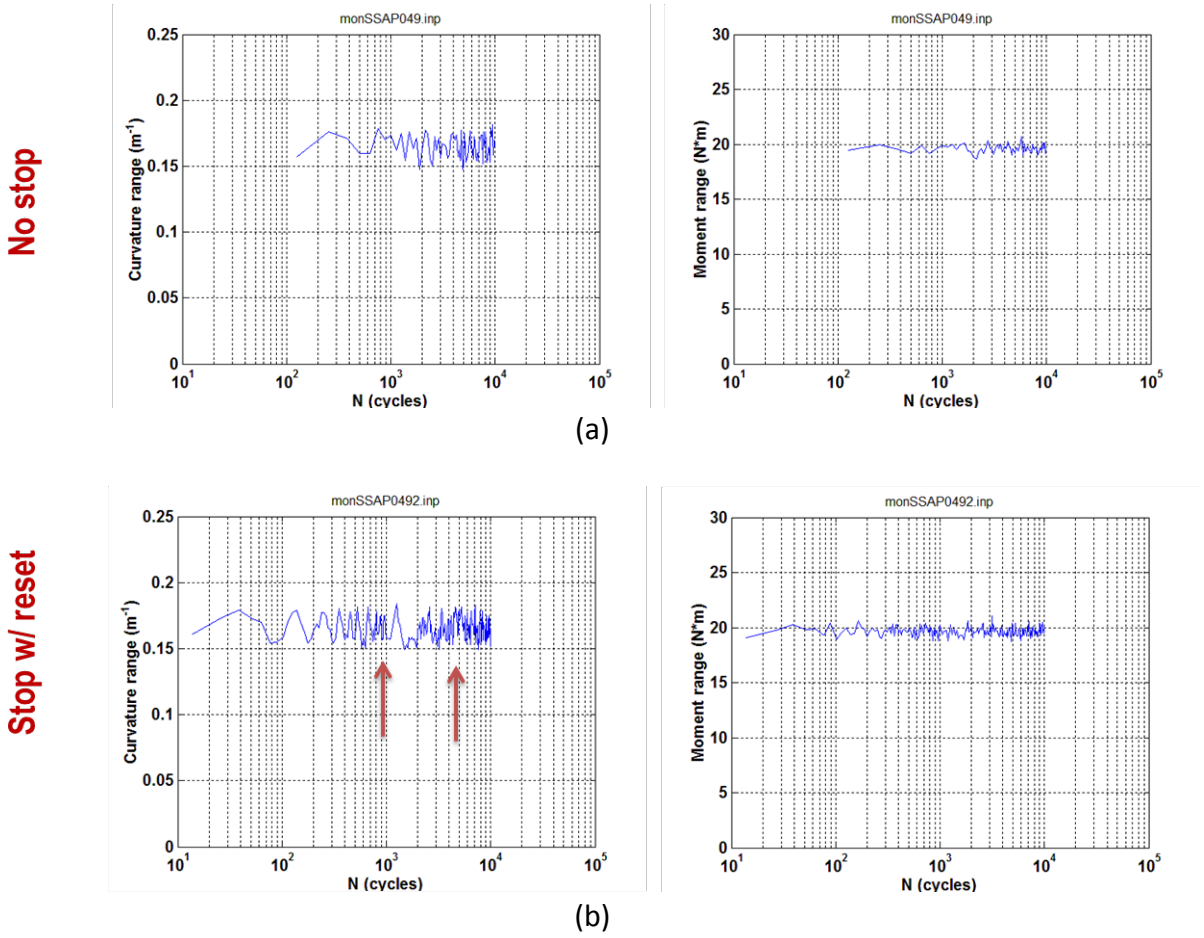

Figure 13. No significant changes in curvature response observed between (a) procedure 1 and (b) procedure 3 for chisel head contact.

The zero-N end-level control was tested to more than 100,000 cycles at 5 Hz (Table 3), where the measurements were accomplished using relative displacement control; that is, the cyclic test was stopped at each designated number of cycles. The test results showed no significant discontinuity related to measurement stops for curvature changes. Thus, zero-N end-level control is a reasonable procedure to use during testing (Figure 14).

Table 3. Test procedure with zero-N end-level control using chisel contact. Relative displacement control was used.

Date	No.	pk1 (mm, N)	pk2 (mm, N)	Freq (Hz)	Increment	Total cycles	Note
1/16/2014	29	-100	100	5	1000	1000	zero N
1/16/2014	30	-0.3	0.3	0.05	3	1000	rel. displacement
1/16/2014	31	-0.4	0.4	0.05	3	1000	rel. displacement
1/16/2014	32	-0.5	0.5	0.05	3	1000	rel. displacement
1/16/2014	33	-100	100	5	10000	11000	zero N
1/16/2014	34	-0.3	0.3	0.05	3	11000	rel. displacement
1/16/2014	35	-0.4	0.4	0.05	3	11000	rel. displacement
1/16/2014	36	-0.5	0.5	0.05	3	11000	rel. displacement
1/16/2014	37	-100	100	5	100000	111000	zero N
1/17/2014	38	-0.3	0.3	0.05	3	111000	rel. displacement
1/17/2014	39	-0.4	0.4	0.05	3	111000	rel. displacement
1/17/2014	40	-0.5	0.5	0.05	3	111000	rel. displacement

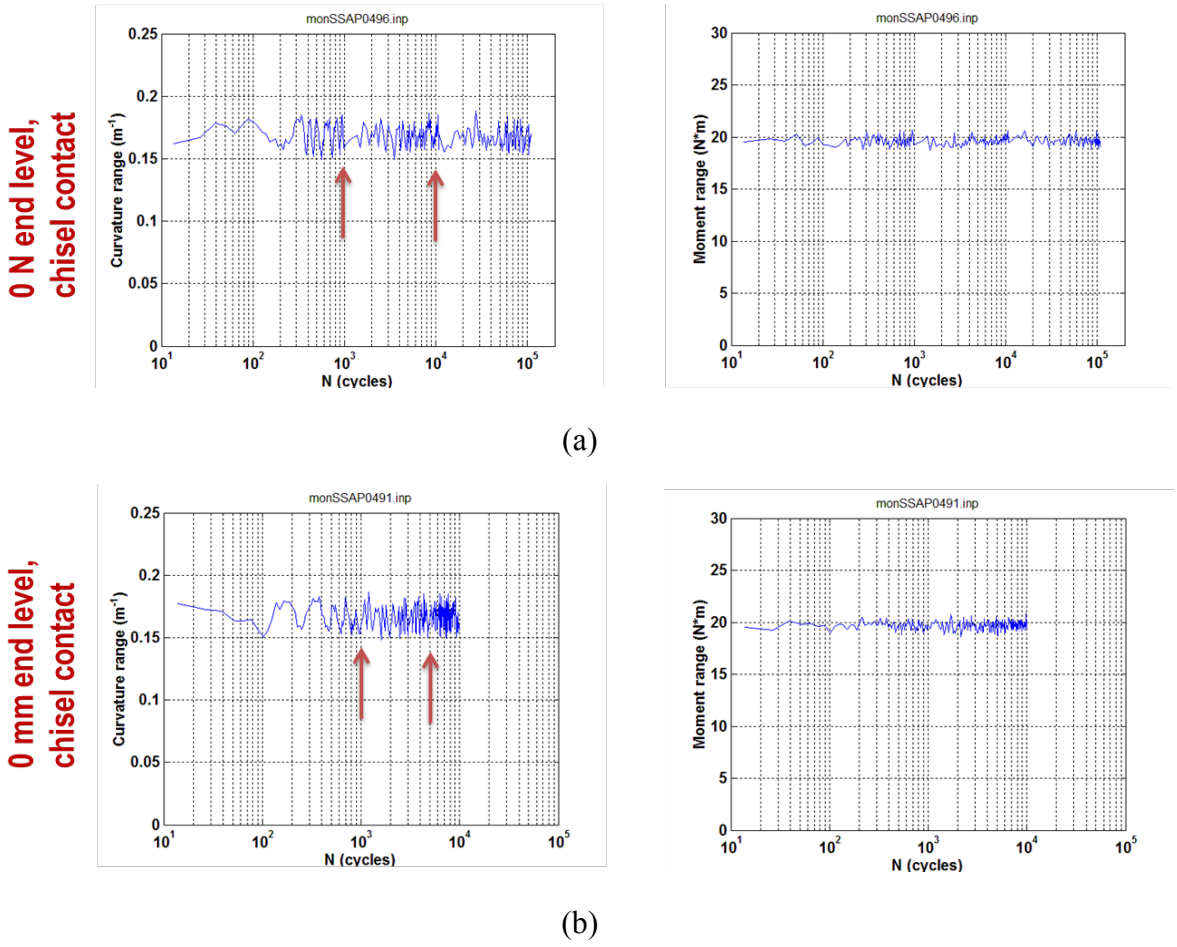

Figure 14. No significant discontinuity was observed near stops during evaluation of curvature variation for (a) zero-N end-level control and (b) zero-mm end-level control.

2.8 Smoothing of Curvature Data

The three LVDT-based curvature measurement system experienced noise distortion during hot-cell testing, making data collection difficult. To resolve this problem, low-frequency measurement data collected during hot-cell testing were studied by using a least-squares splice smoothing function. A MATLAB-based cubic 15-piece approximation function was used to smooth a 70-second data block obtained during testing at 0.05 Hz. The data processing procedure consisted of the following steps:

1) smooth the moment data,
2) smooth the three LVDT signals,
3) reset the three LVDT channels after smoothing,
4) calculate the curvature based on the reset three LVDTs, and
5) smooth the curvature data.

Preliminary smoothed moment and curvature data are shown in Figure 15 and Figure 16. The data show that re-setting the LVDT channel in WinTest would not be effective because of the large noise level. The initial trigger level can be very different from the reset near zero level as seen in the case of LVDT1

(Figure 17). Therefore, a reset to the true mean level based on the smoothed LVDT signal was necessary to provide reproducible and reliable information during data processing. The effect of resetting LVDTs and smoothing the data can be seen clearly in the moment-curvature hysteresis loops in Figure 18. The adjusted moment-curvature curve provides more accurate test results that show the symmetrical dynamic response from CIRFT testing.

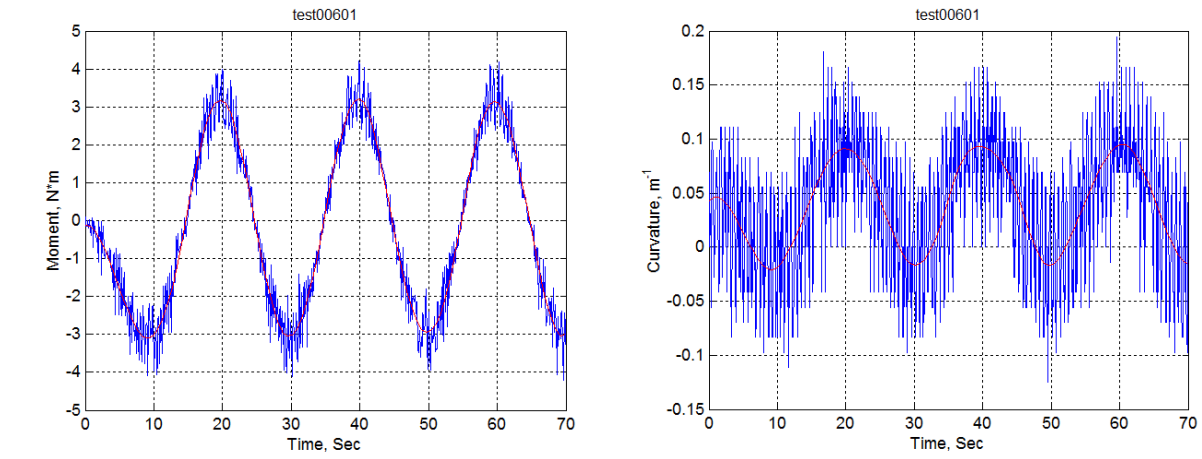

(a) (b)

Figure 15. (a) Moment and (b) curvature data smoothed by using a cubic 15-piece approximation function.

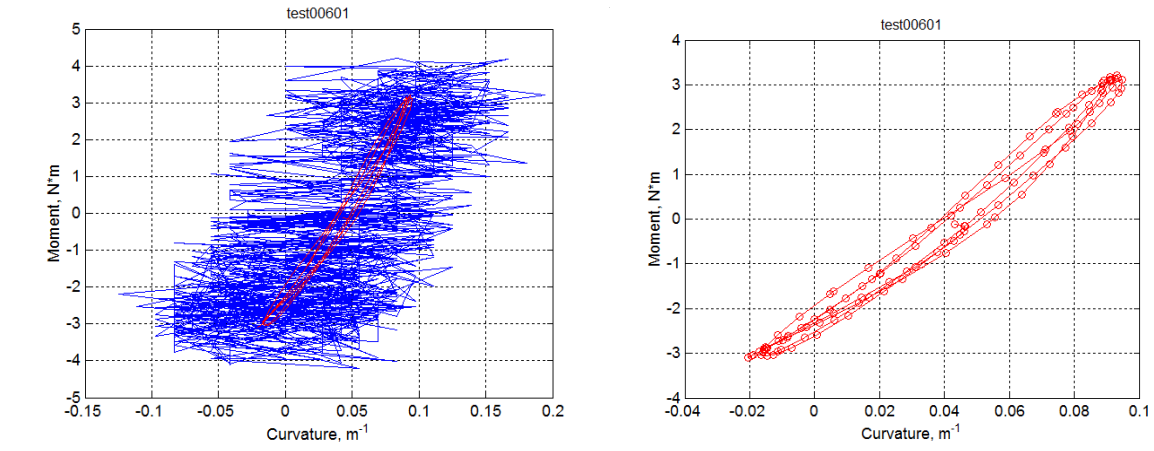

(a) (b)

Figure 16. (a) Noisy and (b) de-noised moment-curvature curve.

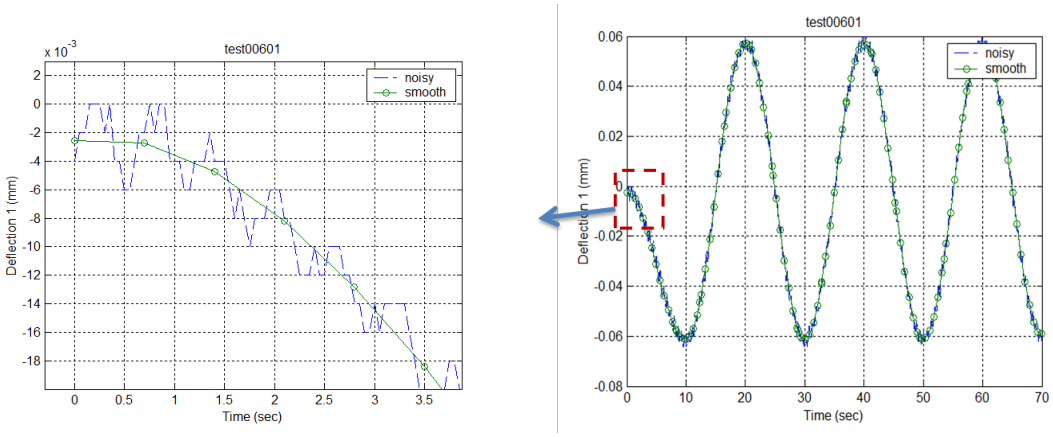

(a) (b)

Figure 17. (a) Enlarged initial stage of LVDT1 data, and (b) the data block obtained in one measurement session.

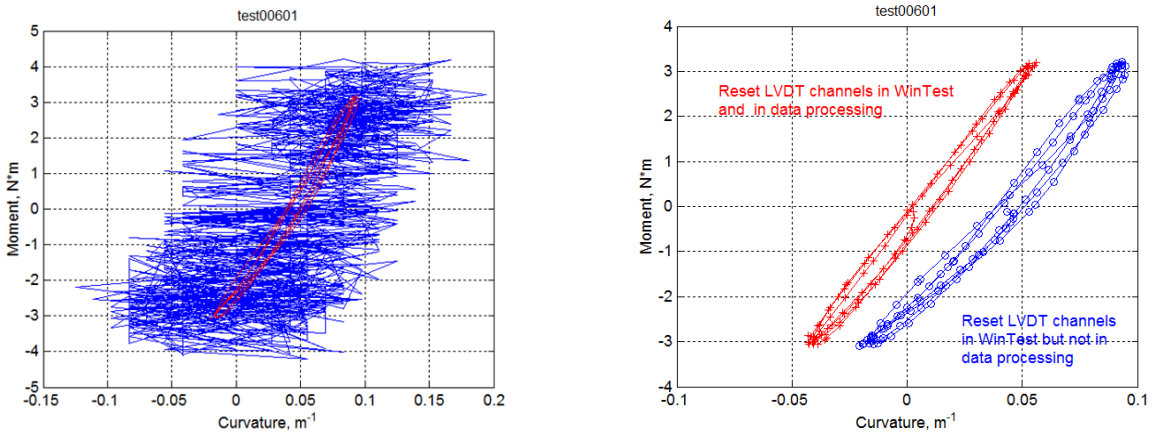

(a) (b)

Figure 18. (a) Measurement with noise (blue) and with noise removed (red) and (b) same measurement after resetting the smoothed three LVDT channels and smoothing the curve.

2.9 Test System Analysis

The resistance of the CIRFT system components as they affect the actual driving force of the dual linear motors was evaluated, during low-amplitude cyclic testing. The potential effects of this resistive force were evaluated by testing a surrogate rod in the out-of-cell CIRFT machine.

The surrogate rod was made of a SS304 tube with ID 7.874 mm, OD 9.563 mm, E = 193 GPa, and EI = 42.8 Nm^2. The tests were conducted under ±100N, 1 to 10 Hz to evaluate the response of the CIRFT

system. Two series of the tests were conducted to examine the repeatability of the data. One set of input-output data is shown in Figure 19; part of the data was smoothed and then used in this evaluation. The curvature range as a measure of the response of the input moment is shown in Figure 20. Because the rigidity (EI) of the rod is given, the curvature can be converted into the moment actually applied to the rod. Thus, the moment applied to the rod and the moment applied to the U-frame can be correlated. The results are expressed in terms of gain, the ratio of moments of the rod to the U-frame, as shown in Figure 21. The data are very repeatable, and the gain is close to one at the 5 Hz testing level that is being used during the current hot-cell cyclic testing. Future measurements will be made to ensure that system resistance does not increase over time.

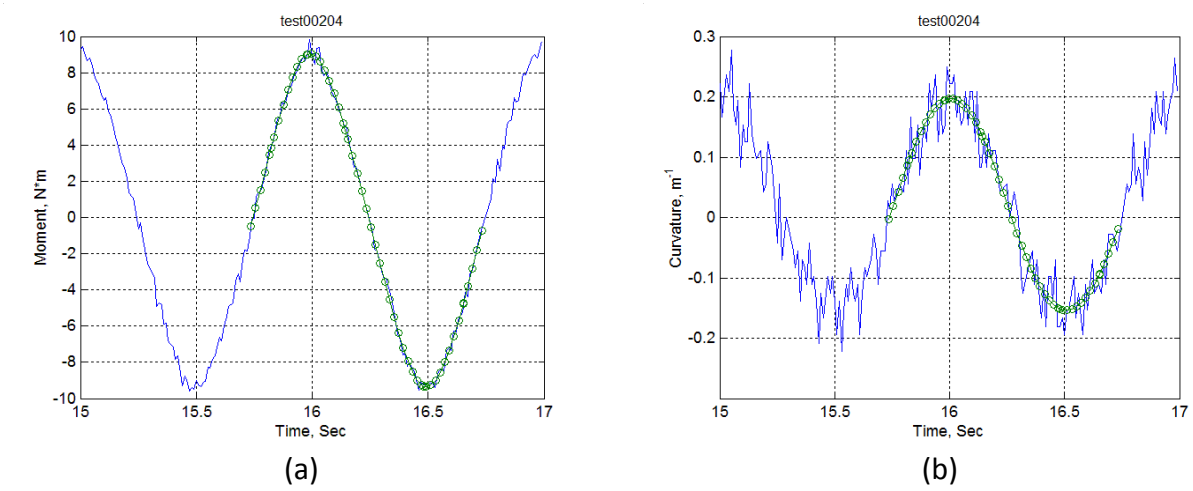

Figure 19. (a) Applied moment and (b) curvature based on test at 1 Hz. Smoothing has been applied to both signals. One-period data block was used in the characterization.

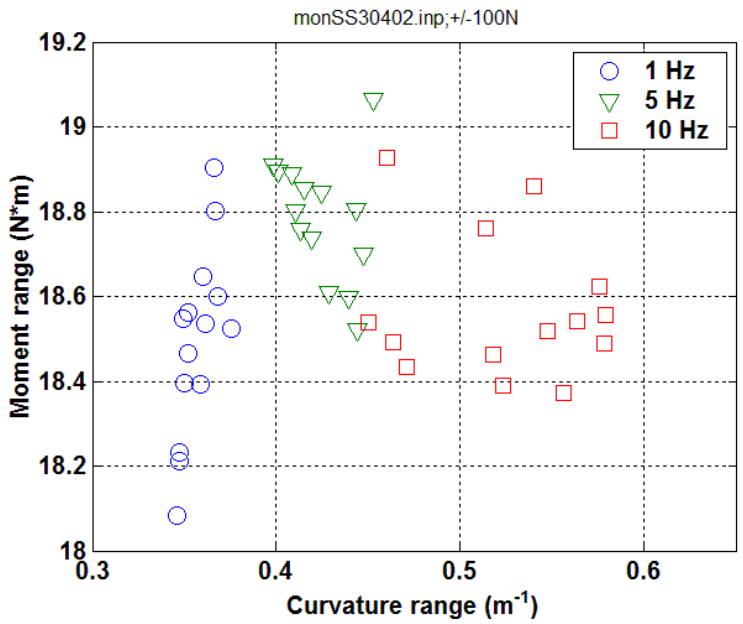

Figure 20. Scatter plot of moment range vs. curvature range based on the first test run.

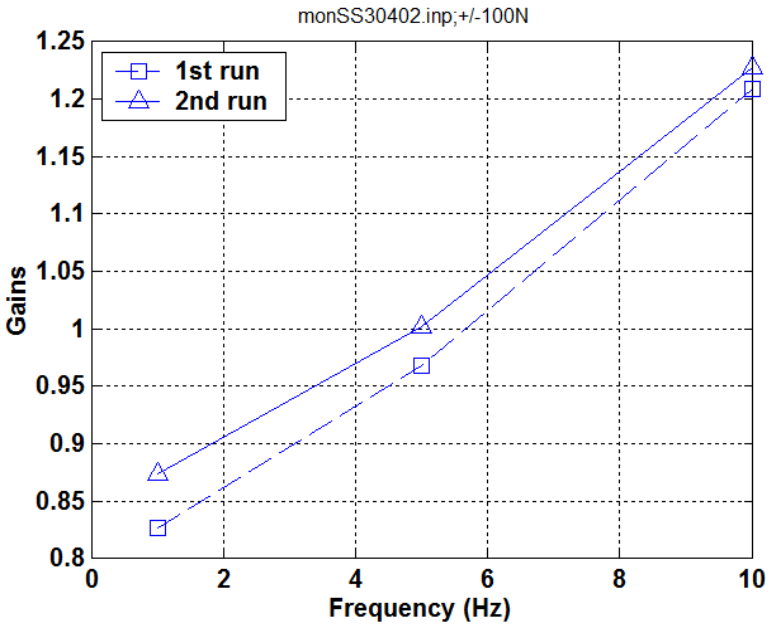

Figure 21. Gain as a function of frequency.

2.10 Conclusion

An out-of-cell CIRFT system has been assembled with the same configuration as the CIRFT system that is being used in hot-cell testing. A number of hot-cell adaptions (such as cabling modifications) have not been made to the out-of-cell CIRFT since this equipment will be used in out-of-cell testing until needed for use in the hot cell.

Current out-of-hot-cell testing provided the following information, reflecting the accuracy of the CIRFT system.

- No significant probe head contact effect was observed on the curvature response of test specimens.
- No significant effects of test stops and channel resets were observed.
- No significant effect of ending control was seen on the curvature response with respect to displacement and load control.
- Curvature measurements can be improved in small amplitude measurements by using noise smoothing.
- When using a calibration rod with known properties, the dynamic response of the CIRFT in the target frequency range was studied. The gain can be defined but may be dependent on the calibration rod used.

This page intentionally left blank

3. FINITE ELEMENT ANALYSES

3.1 Background

The FEA was used to investigate the impacts of interfacial bonding efficiency at both the pellet–pellet and pellet–clad interfaces on UNF vibration integrity. The FEA simulation results were then validated with reverse bending fatigue tests on surrogate rods consisting of stainless steel (SS) tubes with alumina-pellet inserts. Bending moments (M) were applied to the FEA models to evaluate the system response of the surrogate rods. From the induced curvature, κ, the flexural rigidity EI is estimated as $EI = M/\kappa$. The impacts of interfacial bonding efficiency on UNF vibration integrity include the moment carrying capacity distribution between pellets and clad and the impact of cohesion between the pellets and the clad on the flexural rigidity of the surrogate rod system.

3.2 Introduction

For high-burnup UNF, the fuel pellets and clad can be fused together to form an integrated UNF system. To understand the underlying mechanism of pellet–pellet and pellet–clad interface dynamics in a transportation environment, it is essential to accurately evaluate the mechanical properties of the integrated UNF system. Prior to conducting physical experimentation on high-burnup UNF, a series of FEA protocols have been developed to investigate UNF vibration integrity using a surrogate rod system that resembles a UNF composite rod system to establish qualitative as well as quantitative assessments of UNF rod system performance under normal UNF transportation conditions.

The FEA models of a surrogate rod system use alumina pellets and SS tubing with the appropriate boundary conditions, including bonded epoxy at the clad/pellet interfaces. The model consists of a surrogate rod with 3D representation of fuel pellets, clad, and possible combinations of the gaps at the pellet–pellet and pellet–clad interfaces. The ABAQUS code was used in the FEA, and the surrogate rod was represented by the beam element with the associated effective stiffness. This approach was used to obtain the beam element properties that would be most effective as input for further development of the detailed UNF assembly model. The approach is also designed to estimate the damping properties of the beam elements due to frictional resistance between the clad and embedded pellets. This pellet–clad interaction modeling uses a “contact element” algorithm and can be further implemented into other embedded boundary conditions, such as internal pressure and residual stress, etc.

The FEA evaluation provides detailed explanations on the effects of pellet–pellet and pellet–clad interactions, including pellet fracture and pellet–clad bonding efficiency, on clad performance reliability under normal continuous transport. The FEA simulation results provided input to support subsequent out-of-cell CIRFT testing. The CIRFT data [11, 12] was then used for calibration and benchmarking of future FEA evaluations.

The FEA models, with a 50.8 mm (2 in.) gauge section that covered the SS clad and alumina pellets with epoxy layers supplying cohesion, were developed with the ABAQUS code. In order to estimate the surrogate rod system responses including the stress profile and the associated curvature, κ, the bending moments (M) were applied to both ends of the surrogate rod. From the FEA results, the flexural rigidity (EI) of the simulation cases is estimated as $EI = M/\kappa$. Detailed discussions and comparisons of the simulation cases are organized as follows.

1. The section model with good interfacial bonding and without pellet fracture
2. The section model with good bonding at pellet–clad interfaces and de-bonding at pellet–pellet interfaces
3. The section model with de-bonding both at pellet–clad and pellet–pellet interfaces

The simulation results indicate that the system response and the associated flexural rigidity are strongly dependent on the interfacial bonding efficiency.

3.3 Analysis of Interfacial Bonding Efficiency of Surrogate Rods

Structural analysis and an interfacial bonding evaluation of the surrogate rods used in the bending fatigue testing system [11–13] were performed with the ABAQUS code. The CIRFT used surrogate rods to calibrate and improve the test setup in an out-of-cell environment. To validate simulation results with out-of-cell surrogate data, the surrogate rod materials used in the FEA were the same as those used in the out-of-cell testing. High-density alumina was selected as the pellet material, and SS 304 was used as the clad material. Epoxy was used as the interfacial bonding material. The material properties of the surrogate test rods are listed in Table 4.

Table 4. Material properties of surrogate rods

Material	Young's Modulus (psi)	Poisson's Ratio	Yield Strength (psi)	Density (lb/in^3)
Stainless Steel[a]	2.800×10^7	0.300	4.206×10^4	0.2901
Al_2O_3[b,c]	5.395×10^7	0.220	3.626×10^5	0.1416
Epoxy[d,e]	5.076×10^5	0.370	1.001×10^4	0.0452

[a]Product Data Bulletin, 304/304L stainless steel, AK Steel Corporation, http://www.aksteel.com
[b]Ceramic Properties Standard, CoorsTek, Inc., http://www.coorstek.com
[c]The mean flexural strength of the Al_2O_3 is around 48 ksi from the vendor McMaster-Carr.
[d]More about Glass, Ceramics, Carbon; more About Stainless Steel Alloys, Mechanical and Physical Properties, http://www.mcmaster.com
[e]http://www.engineeringtoolbox.com/material-properties-t_24.html

3.3.1 Rods with Good Interfacial Bonding

Figure 22 shows the geometry of a U-frame bending fatigue testing system with a co-planar configuration for the surrogate rod. The 2-in. gauge section is highlighted in black. A finite element model was established to represent the 2-in. gauge section of the test specimen, referred to as the Clad-Epoxy-Pellet section model (Figure 23), and shows the cross-sectional and longitudinal cut views of the 2-in. surrogate rod. The inside and outside diameters (ID and OD) of the clad are 0.382 and 0.436 in., respectively. The alumina pellet OD is 0.372 in. The 2-in. gauge section of the surrogate rod contains two 0.6-in. pellets in the middle and two 0.4-in. pellets at the ends. This use of two pellet sizes provides model symmetry while placing the area of interest in the middle of the gage section. The gap between the clad and the pellet was 0.005 in. and was filled with a cast epoxy layer. The extent of epoxy filling and bonding apparently depends on the casting and the subsequent loading. In this study, three conditions were studied: 1) pellet–clad and pellet–pellet interfaces are bonded, 2) pellet–clad interfaces are bonded and pellet–pellet interfaces are de-bonded, and 3) pellet–clad and pellet–pellet interfaces are both de-bonded.

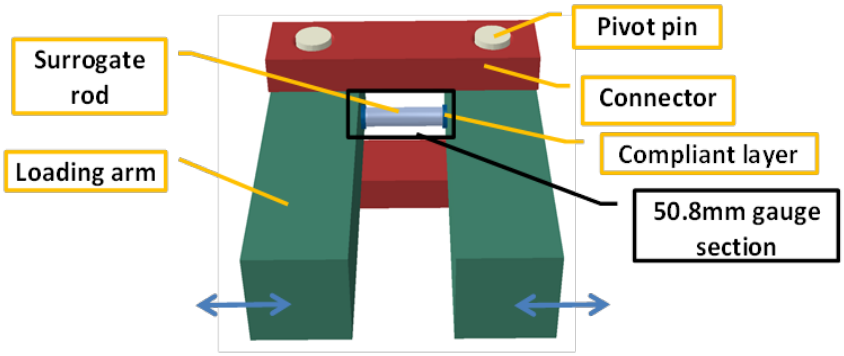

Figure 22. Geometry of horizontal U-frame bending fatigue testing system with co-planar configuration of the rod.

The Clad-Epoxy-Pellet section model with four pellets is shown in Figure 23. Bending moments were applied on both ends of the surrogate rod rotating along the x-axis, as shown in Figure 23 (b). According to the out-of-cell surrogate data, the bending moments ranged from 20 to 30 N·m; the bending moment Mx was selected as 25 N·m. Both loading surfaces of the surrogate rod were constrained with rotation along y- and z-axes and translation along the x direction. In the following finite element models, the global mesh is 0.02 in. Some local meshes are as small as 0.0025 in.

The quasi-static procedure used in FEA is from the ABAQUS code. The original surrogate rod was, in fact, 6 in. long with 10 alumina pellets [12–13]. The contact between neighboring pellets generally depends on the casting process. Gaps may exist between the pellets and may be filled with epoxy. The modeling study in this report considered the following aspects:

1. gaps were filled with epoxy layers in which pellet–epoxy and epoxy–pellet interfaces were tied or bonded,

2. gaps existed and were not filled with epoxy layers, and

3. pellet and pellet in direct contact (no gap) and pellet–pellet interfaces were de-bonded.

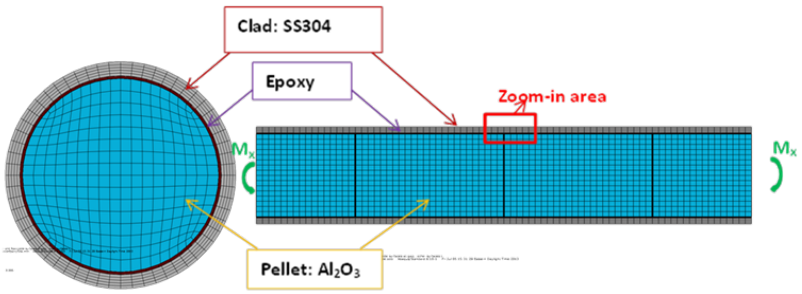

Figure 23. Geometry of Clad-Epoxy-Pellet section model with four pellets.

The configuration of the perfectly bonded case is shown in Figure 22Thin epoxy layers are tied to the gap surfaces at the pellet–clad interfaces and at the pellet–pellet interfaces to simulate cohesive bonding.

This model has three 0.0014-in. gaps filled with epoxy at the pellet–pellet interfaces. The resultant stress distribution and curvature are shown in Figure 25. The resultant curvature is 0.157 m^{-1}, too small to be noticeable, as illustrated in Figure 25(a). From the resultant stress distribution shown in Figure 25(b), the maximum stress occurs at the outer surface of the alumina rod, and the resultant forces also indicate that the alumina pellets carry a larger portion of the moment resistance than the clad. The clad did not yield under a 25 N·m bending moment, nor did the alumina pellet, which has a much higher yield strength than the SS clad. This indicates that the surrogate rod in a perfectly bonded condition will remain within the linear elastic range under the target loading.

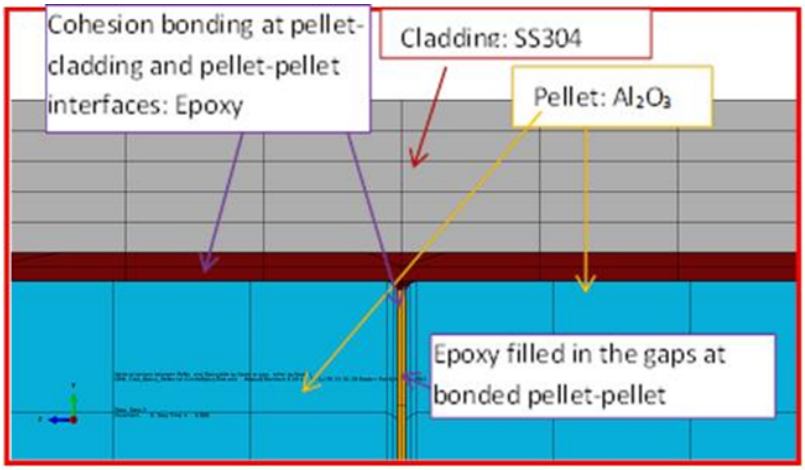

Figure 24. Zoomed-in area for the case of epoxy filling in the gaps at bonded pellet–pellet interfaces.

The curvature and flexure rigidity for this case are summarized in Table 5. In this case, a load control procedure was used, the bending moment M was applied to both ends of the surrogate rod, and the bending curvature κ was estimated from the FEA result within the gage section.

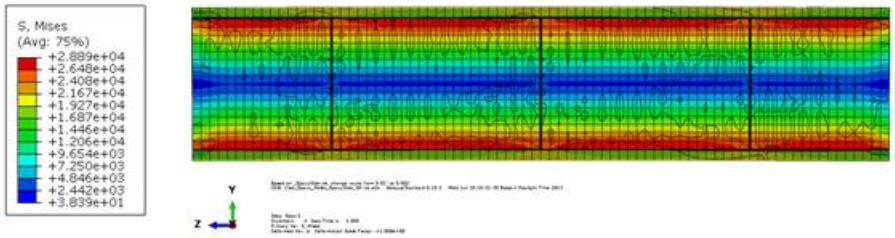

(a) Longitudinal cut view of resultant curvature and von Mises stress

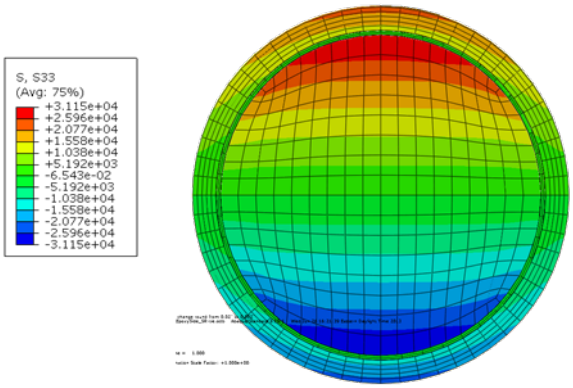

(b) Cross-sectional view of resultant σ_{zz} at a pellet–pellet interface

Figure 25. Normal stress distribution and curvature resulting from Clad-Epoxy-Pellet section model with four pellets and epoxy-filled gaps at pellet–pellet interfaces.

Table 5. Curvature and flexural rigidity for the ideal interfacial bonding simulation

Designation	Curvature, κ (1/m)	Bending moment, M (N·m)	Flexural rigidity, EI (N·m^2)	Note
Clad-Epoxy-Pellet4-Tie-Pellet-Epoxy-Tie-at Gap	0.163	25	153	Gaps between neighboring pellets filled with epoxy; pellet–epoxy and epoxy–pellet interfaces bonded

In surrogate rod SSAP05 [12], alumina pellets were bonded to the SS tube and to each other using epoxy. The SSAP05 specimen was tested up to the 25 N·m bending moment. High flexural rigidity was observed, as shown in Figure 26. The initial (first cycle) test data, which has the highest flexural rigidity on the left side, indicates that the bonds at the pellet–clad and pellet–pellet interfaces should remain intact at the corresponding curvature level. The flexural rigidity of the first test data is very close to the FEA estimation of 153 N·m^2.

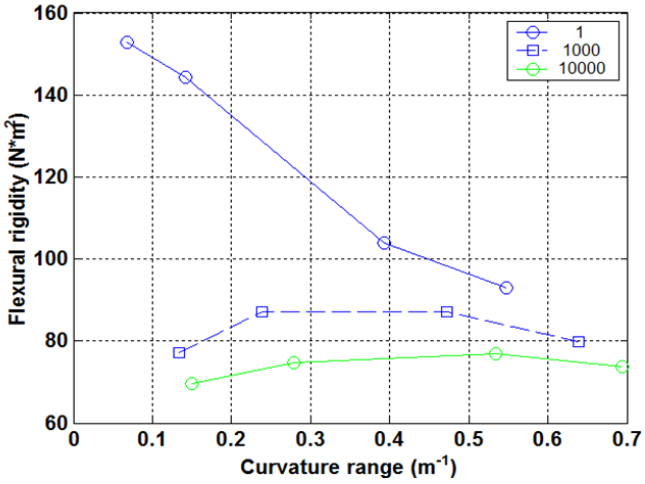

Figure 26. ORNL SSAP05 specimen test data, flexural rigidity vs. curvature measured at various cycle numbers during a bending cycle test [12].

With good interfacial bonding, the alumina rod can carry most of the bending moment under normal transportation vibration because the Young's modulus of the alumina rod is twice that of the clad (Table 4). Due to the high yield strength of the alumina pellets, the surrogate rod can work within the linear elastic range to a large extent. The high flexural rigidity estimated from FEA (Table 5) is in good agreement with that estimated from bending fatigue testing data. Thus, the epoxy layers fully bonded to the surfaces of gaps in both clad–pellet and pellet–pellet directions would capture the earlier elastic behavior of the surrogate rod, and the structural integrity of interfaces should be maintained.

Symmetrical reversible output force was obtained for the composite rod (SS tube + alumina rod) using a U-frame bending fatigue testing system, as shown in . Displacement control was used for bending tests with amplitudes of 0.118 to 0.512 in. (3 to 13 mm) with a frequency of 0.1 Hz, and the deflection was measured at the midpoint of the rod. The composite rod bending test results indicate that before the inserted alumina rod fracture, the composite rod responded linearly and most of the bending load carrying capacity resided on the alumina rod due to a Young's modulus that was twice that of the SS clad. Upon the alumina insert fracture, sudden load transfer occurred and the SS tube started to carry the majority of the bending moment, which resulted in plastic deformation of SS clad, as will be demonstrated in the following simulation cases.

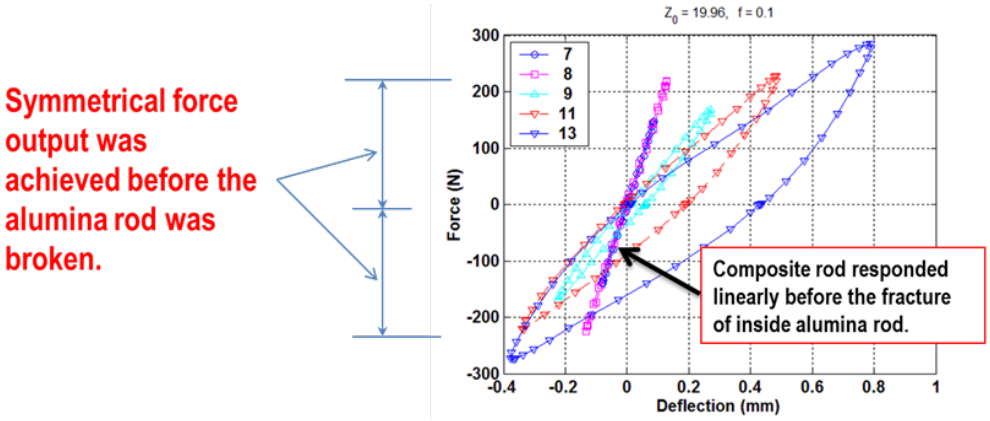

Figure 27. Symmetrical reversible output force obtained for a composite rod (stainless steel tube + alumina rod) using a U-frame bending fatigue testing system with displacement input of 0.1 Hz and amplitude 0.118 to 0.512 in. [11–12].

3.3.2 Effect of Pellet–Pellet Interfacial Bonding Efficiency

Before being transported, the UNF system exhibits inherited stress fields, such as axial tensile stress and tangential tensile stress due to pellet–clad mechanical interaction, or due to oxide volume expansion, as well as radial compressive stress due to hydride compaction and tangential shear stress due to hydride volume expansion. Vibration during transportation will induce reversible bending in a UNF assembly. Repeated expansion and contraction in both the axial and tangential directions of the UNF rod due to reversible bending flexural deformation, combined with stress concentration, can degrade the interfacial bonding at fuel pellet–clad interfaces and pellet–pellet interfaces, as shown in Figure 28. While the shear stress is small relative to the normal stress due to bending, it does not mean that it can be neglected. In particular, in a composite rod or UNF rods, excessive shear due to material mismatch can be a cause of failure for interfacial bonding.

At pellet–pellet interfaces, interfacial bonding fails mainly from normal stress due to reverse bending flexural deformation combined with relatively less shear stress, as shown in Figure 28. At pellet–clad interfaces, localized high shear stress will also arise to compensate for the material mismatch under flexural deformation. As noted above, the shear stress is small relative to the normal stress; thus, it is likely that the interfacial bonding failure at pellet–pellet interfaces will occur before the de-bonding at pellet–clad interfaces. Observation of tests in CIRFT on the surrogate SS rod with alumina pellets verified this hypothesis. In this section, the Clad-Epoxy-Pellet section model with four pellets was used to investigate the surrogate rod bending response with perfect bonding at pellet–clad interfaces, but various de-bonded states at pellet–pellet interfaces were the focus. The material properties, geometry, and loading and boundary conditions are the same as those used in the previous FEA simulation.

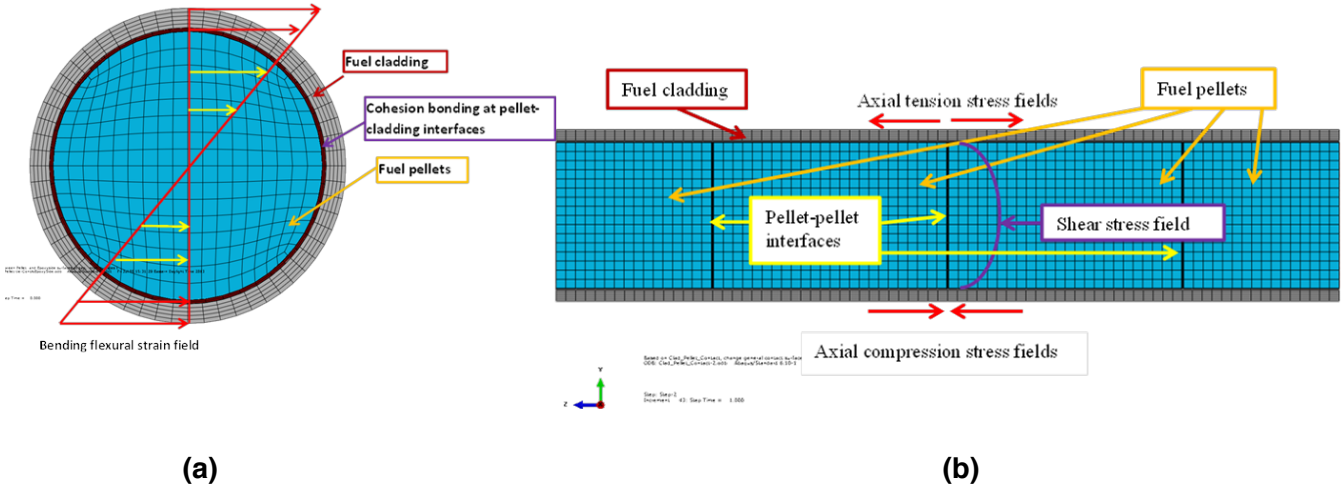

Figure 28. Transportation-induced reversible bending stress fields in a UNF system.

The first case study of pellet–pellet interfacial de-bonding was focused on the gaps at the pellet–pellet interfaces which were all without epoxy, while a thin epoxy layer still existed at all pellet–clad interfaces to provide perfect cohesion between the pellets and the clad.

The stress and curvature responses to the bending moment are illustrated in **Error! Reference source not found.**. Compared to the results shown in Figure 25, there are significant differences in the stress distribution between the case of pellet–pellet interfacial bonding and the case of pellet–pellet interfacial de-bonding, where perfect bonding remains for the pellet/clad wall boundary in cases. For instance, for the pellet–pellet interface of the de-bonded case, the maximum tensile stress, reaching yield strength of clad at 42 ksi occurs within the clad at the pellet-pellet interface region. The curvature profile enlarged 10 times in **Error! Reference source not found.**(b) shows a lateral contraction and lateral expansion at the compression and tension sides of the clad, respectively. Specifically, a localized clad buckle developed near the pellet–pellet gaps, likely due to the lack of internal support. On the compression side, the clad deforms continuously when the pellet–pellet surfaces are being driven together until the gaps are closed. No stress concentrations are observed at pellet–pellet contact corners. Resultant σ_{zz} clearly indicates that the intensely stressed clad takes over more bending moment resistance than that of the pellets at the de-bonded pellet–pellet interfaces.

At the de-bonded pellet–pellet interfaces, the pellets can only transfer load via hard contact, so the load carrying capacity shifts significantly from pellets to the clad. The SS tube starts to carry the majority of the bending moment at the tension side near the pellet–pellet interface region, which results in a significant localized plastic deformation at the SS clad. Over most of the gauge section, the pellets still provide sufficient internal support to the clad due to good cohesion at the pellet–clad interfaces and will carry most of the bending load; therefore, there is no yielding at most regions of the SS clad. The results are contrary to the results of the perfectly bonded case in **Error! Reference source not found.**, which shows that the pellets carry significant bending moment resistance; the maximum stress resides at the pellets, and there is no yielding at either the pellets or the clad.

It was important to note that the von Mises stress distribution in the de-bonded pellets case appears to be in a dog-bone shape due to contact pressure at pellet–pellet interfaces. This also differs from the results of

the bonded pellet–pellet interface case. A third discrepancy lies in the induced curvature. In the de-bonded case, the resultant curvature is 0.669 m^{-1}, which is four times that of the perfectly bonded case shown in Figure 25.

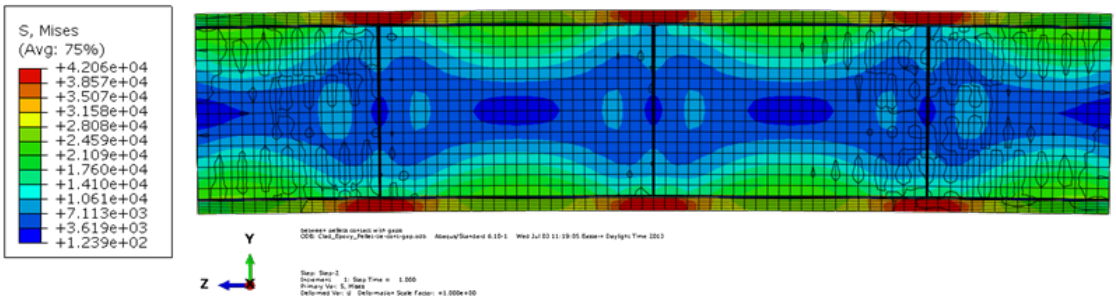

(a) Longitudinal cut view of resultant curvature and von Mises stress

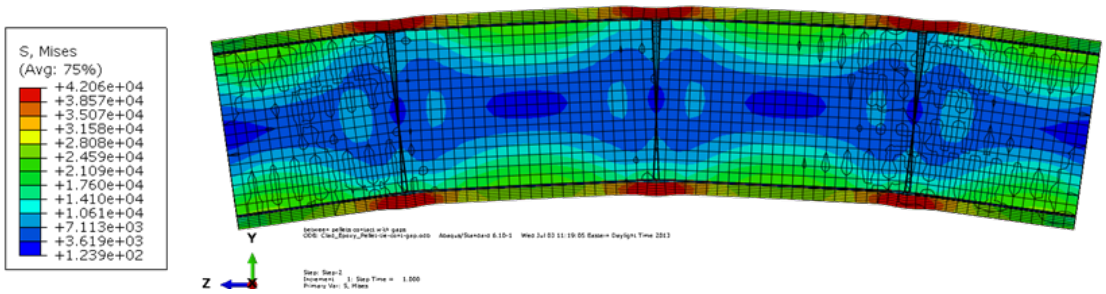

(b) Longitudinal cut view of curvature enlarged by 10 times

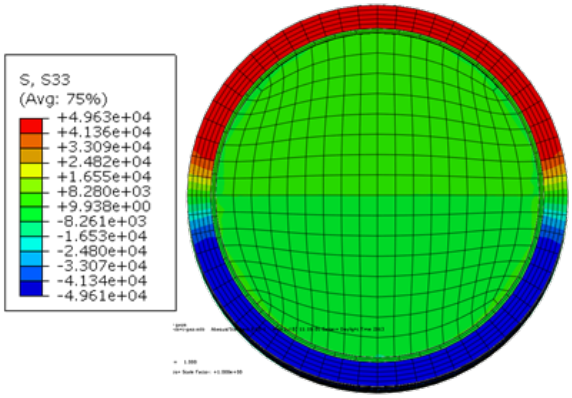

(c) Cross-sectional view of resultant σ_{zz} at a pellet–pellet interface

Figure 29. Stress distribution and curvature resulting from Clad-Epoxy-Pellet section model with four pellets with gaps at de-bonded pellet–pellet interfaces.

The second case on the de-bonded pellet–pellet interface is no gap at pellet–pellet interfaces before applying a bending load. As in previous cases, a thin epoxy layer is applied and tied to surfaces at pellet–clad interfaces to simulate good cohesive bonding.

As illustrated in **Error! Reference source not found.**, the stress distribution of this case appears to be similar to that with gaps between the de-bonded pellet–pellet interfaces. The SS clad also yields at the top tensile side near the pellet–pellet interface regions; however, on the compression side, the maximum

stress occurs at the pellets instead of clad. Nevertheless, the pellet is within the linear elastic range overall due to its high yield strength. From the curvature profile, no clad buckling is observed at the bottom (compression) region. This is because of the absence of gaps at the pellet–pellet interface region; thus, the compacted pellets provide good internal support to the clad tubing structure. Furthermore, pellets seem to carry a significant portion of bending moment resistance via pellet–pellet interaction (pinching at pellet corners), which significantly mitigates the stress level of the clad at the bottom (compression) region.

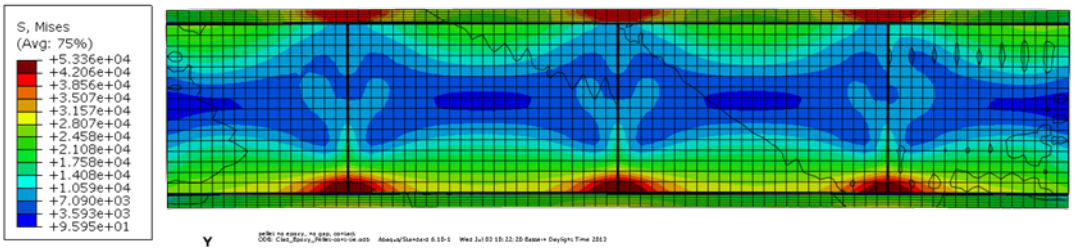

(a) Longitudinal cut view of resultant curvature and von Mises stress

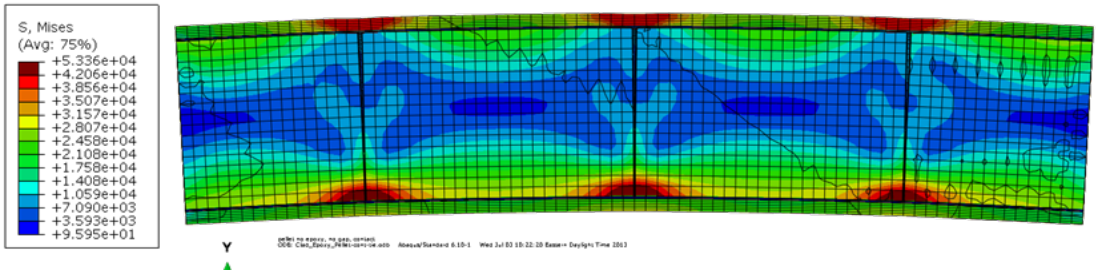

(b) Longitudinal cut view of curvature enlarged by 10 times

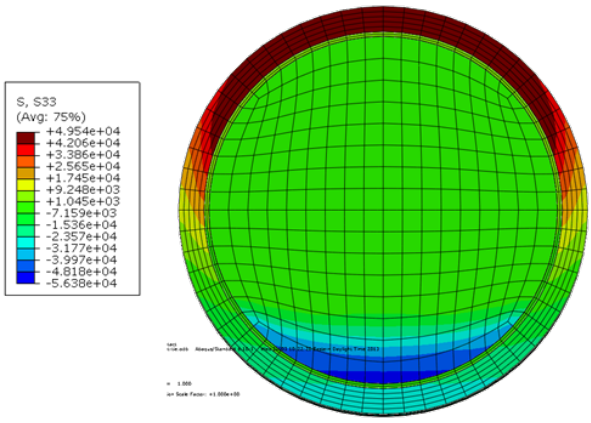

(c) Cross-sectional view of resultant σ_{zz} at a pellet–pellet interface

Figure 30. Stress distribution and curvature resulting from Clad-Epoxy-Pellet section model with four pellets with no gaps at de-bonded pellet–pellet interfaces.

The pellet stress profiles also show a dog-bone shape due to contact pressure at the pellet–pellet interfaces. The resultant σ_{zz} profile with no gaps at the pellet–pellet interface indicates that these pellets

can carry more bending moment resistance than pellets with gaps, as shown in **Error! Reference source not found.**. The induced curvature of this pellet–pellet interface de-bonding with gaps case is 0.241m^{-1}, which is much smaller than that of previous cases.

Table 6 summarizes the estimated curvature and the flexural rigidity based on the two pellet–pellet interface cases discussed in this section. Comparison of the results in Table 2and Table 3 suggests that the immediate consequence of the de-bonded pellet–pellet interface is a significant increase in curvature, and this, in turn, results in a significant reduction in the estimated flexural rigidity. This phenomenon is primarily due to the load carrying capacity shifting from the pellets to the clad.

Table 6. Curvature and flexural rigidity for the bonded pellet–clad and de-bonded pellet–pellet cases

Designation	Curvature, κ (1/m)	Bending moment, *M* (N·m)	Flexural rigidity, *EI* (N·m^2)	Note
Clad-Epoxy-Pellet4-Tie-Pellet-Contact-Gap	0.669	25	37	Gaps between neighboring pellets had no epoxy filling
Clad-Epoxy-Pellet4-Tie-Pellet-Contact-No Gap	0.241	25	104	No gap between neighboring pellets; pellet–pellet interfaces were de-bonded

Table 6 shows that the gaps at pellet–pellet interfaces play a critical role in estimating the flexural rigidity of the surrogate rod. The induced curvature of 0.669 m^{-1} for the case of gaps is four times that of the perfectly bonded interface case. The curvature increase corresponds to a 76% reduction in flexural rigidity, from 153 N·m^2 for the perfectly bonded interface case to 37 N·m^2 for the case of empty gaps. When the gaps are eliminated, the flexural rigidity value can go as high as 104 N·m^2. The above indicates that the gap-induced large plastic deformations of SS clad at the pellet–pellet interface region can lead to significant reduction in the bending stiffness, or, the flexural rigidity (EI) of the surrogate rod system. If there are no gaps at the pellet–pellet interfaces, the pellets can carry a significant portion of bending moment resistance via direct pellet–pellet contact (interaction) to mitigate the potential yield of the clad.

3.3.3 Effect of Gaps Between Pellets with De-Bonded Pellet–Clad Interfaces

Under a flexural deformation, high shear stress will arise at pellet–clad interfaces to compensate for the material mismatch, in addition to the flexural shear stress in the UNF system. Thus, under a reversible bending load during normal transportation, both cyclic normal stress and shear stress can further degrade the interfacial bonding at fuel pellet–clad interfaces. In this section, de-bonded pellet–clad interfaces and de-bonded pellet–pellet interfaces cases are investigated using a Clad-Epoxy-Pellet section model with four pellets. The surrogate rod consisting of SS clad and alumina pellet inserts is used to study the system response to bending moment with de-bonded interfaces. Loading and boundary conditions are the same as those of the previous cases, and the assigned bending moment is 25 N·m.

The first simulation case of interfacial de-bonding is at both pellet–clad and pellet–pellet interfaces. There are empty gaps at the de-bonded pellet–pellet interfaces and a thin epoxy layer at the de-bonded pellet–clad interfaces.

The resultant stress distribution shown in **Error! Reference source not found.** indicates that the yielded SS clad almost extends throughout the whole gauge section, when the interfacial de-bonding occurs at both pellet–clad and pellet–pellet interfaces. This is in great contrast to the results shown in **Error! Reference source not found.**, where the SS tube only locally yields at pellet–pellet interface regions and the maximum stress resides at pellets on the compression side of pellet–pellet interfaces. The pellets were all below yield at the maximum stress level due to high yield strength. The pellet stress contours also show a dog-bone shape due to pellet–pellet contact interaction. The induced curvature of 0.727 m^{-1} is large enough to be visualized from the longitudinal cut view without increasing the scale. It suggests that because of the interfacial de-bonding at both pellet–clad and pellet–pellet interfaces, the contained pellet inserts and the SS clad can only make contact at the pellet–pellet and pellet–clad interface regions, and the pellets cannot provide direct internal support to the clad. Therefore, the load shifts significantly from pellets to the clad over the entire gauge section; the results also indicate that the SS clad carries the majority of the bending moment. The bending deformation in the de-bonded pellet–clad region will likely result in further pinching action at pellet–clad interfaces, which may also result in an accelerated aging of the clad tubing.

The second case is where a thin epoxy layer is filled at de-bonded pellet–clad interfaces and the pellets are all in direct contact with each other with no gaps at the pellet–pellet interfaces. The loading and boundary conditions as well as material properties are the same as those of the previous cases. **Error! Reference source not found.Error! Reference source not found.** illustrates the surrogate rod responses to the bending moment upon interfacial de-bonding without gaps at the pellet–pellet interfaces. The longitudinal cut view shows that the SS clad yields at the top (tension) region throughout the gauge section but remains elastic at the bottom (compression) region. The maximum stress still occurs on the compression side of the pellet region where the pellets are pinching each other. Figure 32 shows interfacial results similar to those observed in **Error! Reference source not found.** for the bonded pellet–clad interfaces and de-bonded pellet–pellet interfaces without gaps. The pellets carry a large portion of the bending moment resistance via pinching pellet corners and reduce the stress intensity of the bottom (compression) portion of the clad. The major difference from the results in Figure 30 is the extensive plastic deformation observed at the top region of the SS tube throughout the entire gauge section, instead of the localized yielding observed at the interface region in Figure 30. Due to the lack of a direct load transferring mechanism from pellet to clad or vice versa because of de-bonded pellet–clad interfaces, the clad takes over the majority of the bending moment resistance.

The results of the curvature and flexural rigidity for the cases of de-bonding at pellet–clad and pellet–pellet interfaces are listed in Table 7. Compared to the results of the de-bonded pellet–pellet interface case listed in **Error! Reference source not found.**, the flexural rigidities are further decreased by 8% (from 37 $N \cdot m^2$ to 34 $N \cdot m^2$) for pellets with gap cases and by 19% (from 104 $N \cdot m^2$ to 84 $N \cdot m^2$) for pellets with no gap cases. This result further validates the earlier hypothesis in the case of pellet–clad interfaces, that interfacial bonding efficiency can significantly affect the flexural rigidity of the surrogate composite rod.

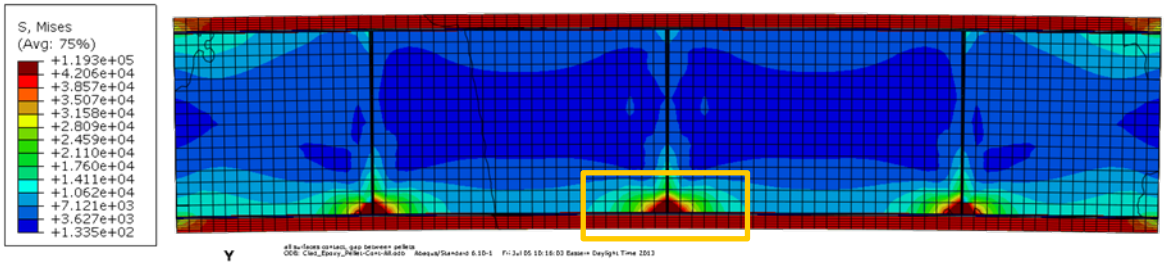

(a) Longitudinal cut view of resultant curvature and von Mises stress

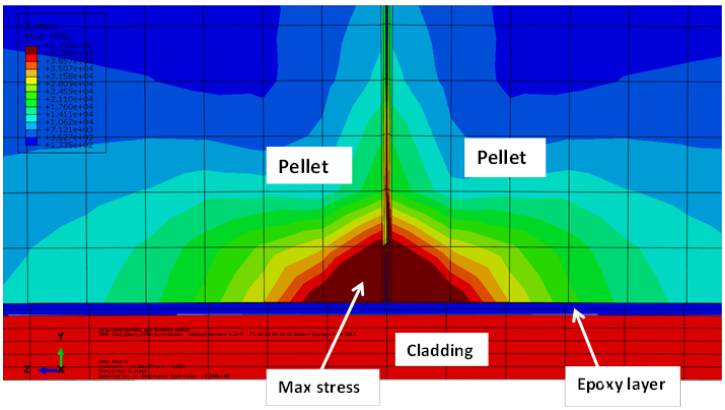

(b) Zoomed-in view of stress distribution at pellet–clad pinning region

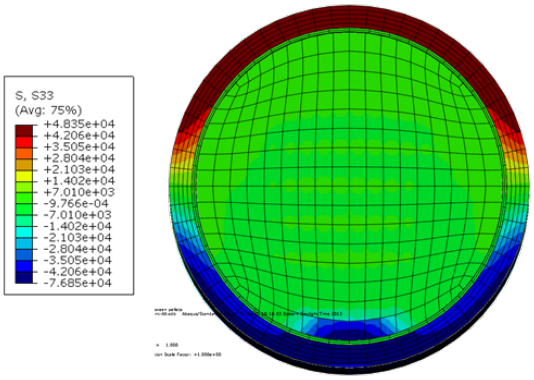

(c) Cross-sectional view of resultant σ_{zz} at a pellet–pellet interface

Figure 31. Stress distribution and curvature resulting from Clad-Epoxy-Pellet section model with four pellets with gaps at de-bonded pellet–pellet interfaces and an epoxy layer at de-bonded pellet–clad interfaces.

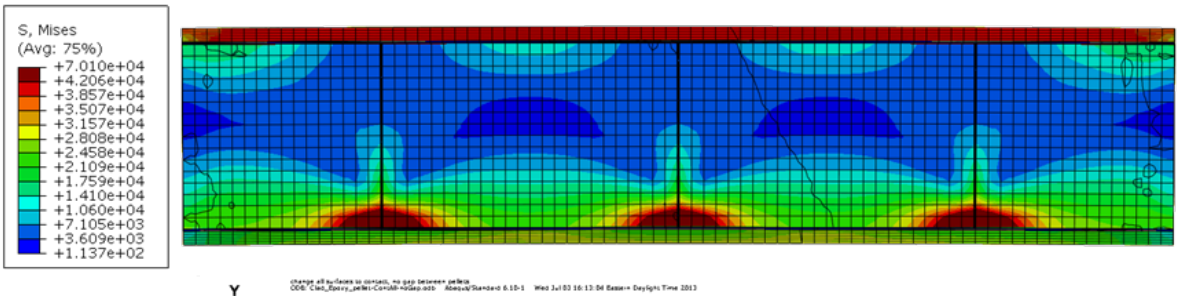

(a) Longitudinal cut view of resultant curvature and von Mises stress

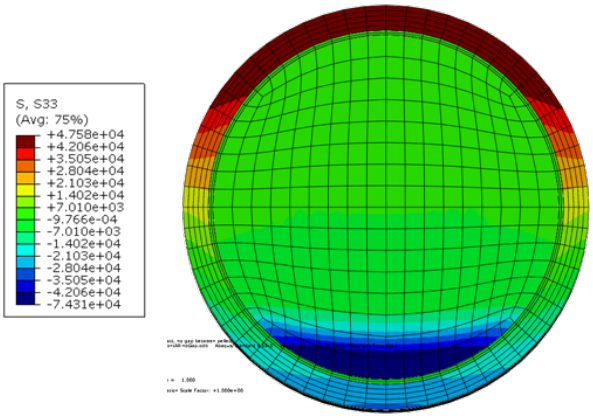

(b) Cross-sectional view of the resultant normal stress, σ_{zz}, at a pellet–pellet interface

Figure 32. Stress distribution and curvature resulting from Clad-Epoxy-Pellet section model with four pellets with no gaps at de-bonded pellet–pellet interfaces and with an epoxy layer at de-bonded pellet–clad interfaces.

Table 7. Curvature and flexural rigidity for de-bonded pellet–clad and pellet–pellet interfaces

Designation	Curvature, κ (1/m)	Bending moment, M (N·m)	Flexural rigidity, EI (N·m^2)	Note
Clad-Epox-Pellet4-Contact-Pellet-Contact-Gap	0.727	25	34	Gaps between neighboring pellets had no epoxy filling
Clad-Epoxy-Pellet4-Contact-Pellet-Contact-No Gap	0.298	25	84	No gap between neighboring pellets; pellet–pellet interfaces were de-bonded

Table 8. Comparison of flexural rigidity between different bonding and de-bonding cases

	Flexural rigidity, *EI* (N·m^2)	Reduction from perfect bonding (%)	Increase from with gaps to without gaps (%)
Perfectly bonded	153	N/A	N/A
De-bonded pellet–pellet interfaces with gaps	37	76	N/A
De-bonded pellet–pellet and pellet–clad interfaces with gaps	34	78	N/A
De-bonded pellet–pellet interfaces without gaps	104	32	64
De-bonded pellet–pellet and pellet–clad interfaces without gaps	84	45	60

In **Error! Reference source not found.**, the flexural rigidity of the case with no gaps at pellet–pellet interfaces is 2.5 times that of the case with gaps. In Table 6, the same comparison of flexural rigidity results in a similar ratio of 2.8. The reason for the large increase in flexural rigidity is the direct contact of the pellets at the pellet–pellet interfaces on the compression side. The direct pellet–pellet contact provides a significant increase in bending moment resistance, resulting in much less curvature deformation.

3.4 Discussion

Based on the FEA simulation results and further verification from ORNL surrogate rod bending test results, the impacts of interfacial bonding efficiency at pellet–pellet and pellet–clad interfaces on surrogate rod system performance can be summarized as follows.

First, with good interfacial bonding and without fuel pellet and clad fracture, the pellets in the surrogate rod will carry more bending moment resistance than the clad under normal transportation vibration. The maximum stress resides at the pellets, and the stresses at the clad and pellet are both below the yield condition; therefore, the system is in a linear elastic state under the target bending loads.

Upon fuel pellet failure including de-bonding at the pellet–pellet interfaces, the load carrying capacity shifts from fuel pellets to the clad, and the clad starts to carry the majority of the bending moment at the pellet–pellet interface region, which results in localized plastic deformation of the clad. With good cohesion at the pellet–clad interfaces, the pellets can still provide support to the clad and carry a sufficient portion of the bending moment resistance, so that a major portion of the clad at the gauge section remains in the linear elastic range.

Upon further de-bonding at the pellet–clad interfaces, the embedded pellets can no longer provide effective structural support to the clad as well as assist the load transfer within the surrogate rod system. Thus, the majority of the load carrying capacity shifts to the clad throughout the entire gauge section. That leads to the clad yielding in the entire gauge section instead of at localized pellet–pellet interface regions. When the pellets contact and pinch each other, the pellets seem to take over a significant portion of the bending load resistance, especially for cases where there are no gaps at the pellet–pellet interfaces. This pellet pinning action certainly mitigates and avoids the clad yielding, and the maximum stress resides at the pellet region and below the yield.

The immediate consequence of interfacial de-bonding is the load carrying capacity shift from fuel to clad, as well as the reduction of flexural rigidity, as shown in Table 8. Compared to the flexural rigidity of 153 $N \cdot m^2$ for a perfect bond, the flexural rigidity for the de-bonding at pellet–pellet interfaces alone is reduced by 76% (to 37 $N \cdot m^2$) in the case with gaps at the pellet–pellet interfaces and by 32% (to 104 $N \cdot m^2$) for the case with no gaps. Upon further de-bonding at the pellet–clad interfaces, the flexural rigidity is further reduced by 8% and 19% for the cases with gaps and without gaps, respectively. The overall reductions from the perfectly bonded case to the de-bonded case at all interfaces are about 78% and 45%, respectively, for the cases with gaps and without gaps.

More reductions in flexural rigidity are due to de-bonding at pellet–pellet interfaces than to de-bonding at pellet–clad interfaces. Table 8 shows about a 60% increase in the flexural rigidity from the case with gaps to the case without gaps, which indicates a significant increase in system stiffness for the surrogate rod without gaps. Therefore, gaps at the interfaces of the surrogate rod system can have a significant impact on system reliability, especially at pellet–pellet interfaces.

The flexural rigidity and bending moment resistance capacity of the surrogate rod system (which is designed to resemble the UNF system) are strongly dependent on the efficiency of interfacial bonding at pellet–clad and pellet–pellet interfaces. This discovery was also validated by CIRFT test results performed on the surrogate SS rod with alumina pellets inserts.

4. REFERENCES

1. J.-A. J. Wang and H. Wang, *Progress Letter Report on Reversal Bending Fatigue Testing of Zry-4 Surrogate Rod (Out-of-Cell Fatigue Testing Development–Task 2.4)*, ORNL/TM-2013/297, Oak Ridge National Laboratory, Oak Ridge, Tenn., August 2013.
2. J.-A. J. Wang, H. Wang, B. B. Bevard, R. L. Howard, and M. E. Flanagan, *Reversible Bending Fatigue Test System for Investigating Vibration Integrity of Spent Nuclear Fuel During Transportation*, PATRAM 2013, DOE/NRC/DOT, San Francisco, Calif., August 18–23, 2013.
3. J.-A. J. Wang, H. Wang, T. Cox, and C. Baldwin, *Progress Letter Report on Bending Fatigue Test System Development for Spent Nuclear Fuel Vibration Integrity Study (Out-of-Cell Fatigue Testing Development–Task 2.4)*, ORNL/TM-2013/225, Oak Ridge National Laboratory, Oak Ridge, Tenn., July 2013.
4. H. Wang, J.-A. J. Wang, T. Tan, H. Jiang, T. S. Cox, R. L. Howard, B. B. Bevard, and M. E. Flanagan, "Development of U-frame Bending System for Studying the Vibration Integrity of Spent Nuclear Fuel," *Journal of Nuclear Materials* 440, 201–213 (2013).
5. J.-A. J. Wang, H. Wang, B. B. Bevard, R. L. Howard, and M. E. Flanagan, "UNF Test System for Bending Stiffness and Vibration Integrity," International High-Level Radioactive Waste Management Conference, Albuquerque, N.M., April 28–May 2, 2013.
6. J.-A. J. Wang, H. Wang, and Ting Tan, *An Innovative Dynamic Reversal Bending Fatigue Testing System for Evaluating Spent Nuclear Fuel Rod Vibration Integrity or Other Materials Fatigue Aging Performance*, ORNL Invention Disclosure 201102593, DOE S-124,149, April 8, 2011. Patent in review, 13/396,413, February 14, 2012.
7. J.-A. J. Wang, H. Wang, T. Cox, and Y. Yan, *Progress Letter Report on U-Frame Test Setup and Bending Fatigue Test for Vibration Integrity Study (Out-of-Cell Fatigue Testing Development–Task 2.3)*, ORNL/TM-2012/417, Oak Ridge National Laboratory, Oak Ridge, Tenn., August 2012.
8. J.-A. J. Wang, H. Wang, T. Tan, H. Jiang, T. Cox, and Y. Yan, *Progress Letter Report on U-Frame Test Setup and Bending Fatigue Test for Vibration Integrity Study (Out-of-Cell Fatigue Testing Development–Task 2.2)*, ORNL/TM-2011/531, Oak Ridge National Laboratory, Oak Ridge, Tenn., January 2012.
9. J.-A. J. Wang, H. Wang, Y. Yan, R. Howard, and B. Bevard, *High Burn-up Spent Fuel Vibration Integrity Study Progress Letter Report (Out-of-Cell Fatigue Testing Development–Task 2.1)*, ORNL/TM-2010/288, Oak Ridge National Laboratory, Oak Ridge, Tenn., January 2011.
10. US Department of Energy, Used Fuel Disposition Campaign, *Used Nuclear Fuel Loading and Structural Performance under Normal Conditions of Transport – Modeling, Simulation and Experimental Integration RD&D Plan*, FCRD-UFD-2013-000135, April 1, 2013.
11. J.-A.J. Wang, H. Wang, Y. Yan, R. Howard, and B. Bevard, *High Burn-up Spent Fuel Vibration Integrity Study Progress Letter Report (Out-of-Cell Fatigue Testing Development – Task 2.1)*, ORNL/TM-2010/288, Oak Ridge National Laboratory, Oak Ridge, TN, 2011.
12. J.-A.J. Wang, H. Wang, T. Tan, H. Jiang, T. Cox, and Y. Yan, *Progress Letter Report on U-frame Test Setup and Bending Fatigue Test for Vibration Integrity Study (Out-of-Cell Fatigue Testing Development – Task 2.2)*, ORNL/TM-2011/531, Oak Ridge National Laboratory, Oak Ridge, TN, 2012
13. H. Wang, J.-A.J. Wang, T. Tan, H. Jiang, T. Cox, R. Howard, B. Bevard, and M. Flanagan, "Development of U-Frame Bending System for Studying the Vibration Integrity of Spent Nuclear Fuel," *Journal of Nuclear Material* **440**, 201–213, 2013.
14. Y. Yan, J. Wang, R.H. Howard, and L.J. Ott, *Post-Irradiation Examination of Zircaloy-4 Samples in Target Capsules and Initiation of Bending Fatigue Testing for Used Nuclear Fuel Vibration Integrity Investigations*, prepared for U.S. Department of Energy Nuclear Fuels Storage and Transportation Planning Project, by Oak Ridge National Laboratory, Oak Ridge, TN, FCRD-UFD-2013-000369, September 30, 2013.

This page intentionally left blank

APPENDIX A

Experiments Test Plan (UFD)

The UFD Experiments Test Plan will help develop information in support of ongoing program modeling efforts and will provide information that may eventually be used to support licensing activities. The test plan includes FEA to inform the program concerning clad/fuel separate effects and combined effects, and hot-cell and out-of-hot-cell testing on irradiated and unirradiated cladding and clad/fuel samples.

This test plan describes recommended tests to be done and a potential order of those tests. However, many of the tests will include elements of FEA, followed by out-of-cell testing and eventually in-cell testing, so that the actual testing will be conducted based on the results of the each previous test. This will allow the program the opportunity to review the results of tests to determine whether to continue with the next planned test or modify the test plan to reflect the new knowledge gained in previous tests.

The planned tests are described below.

Finite Element Analysis (FEA)

Test Description	Reason for Test
1. Utilize NRC experimental data to validate the FEA model. a. Add detail including pellet patterns/shape, transition region information (bonding mechanisms) etc.	Ensure the FEA model represents the actual interface conditions and responses noted in the NRC static and dynamic tests. *Precursor activity – NRC experiments*
2. Use FEA to help understand and quantify CIRFT system performance, including system inertia and system resistance evaluations, to properly filter out and the CIRFT system data biases and uncertainties.	Match out of cell experiments with FEA to understand machine dynamic system performance, including system inertia, alignment as well as bearing system resistance. *Precursor activity – NRC experiments*
3. Establish which clad/fuel mechanical properties are most important to be evaluated in actual testing. a. Fuel chamfer b. Fuel gaps c. Fuel fragmentation (fuel toughness) d. Clad thickness e. Clad ductility (and response to varying amounts of burnup) f. Hydride amount and orientation g. Determine fuel properties independent of the cladding	Use the PIRT report to develop a modeling matrix and conduct FEA on those clad/fuel properties deemed important. Use FEA to vary the various parameters to understand their impacts on the system and how they interact with each other. Conduct FEA to support understanding the hot cell test results and to provide information to inform which future tests (and test conditions) should be conducted. *Precursor activity – None*
4. Develop a PIRT to identify, rank, and understand the clad/fuel properties that are of interest and should be evaluated.	List and understand all the clad/fuel variables that may be of interest to help define what tests are needed and testing priority. *Precursor activity – NRC experiments and FEA of clad/fuel properties.*

Test Description	Reason for Test
5. Conduct FEA to simulate ring compression tests of both fueled and unfueled clad.	These analyses will support out of cell tests that will provide baseline data for in-cell tests. The ring compression results can be correlated and compared to existing ANL data with defueled high burnup samples. The FEA testing will support understanding the optimized length for the (irradiated) clad/fuel sample than can be effectively tested using the ring compression test.
6. Determine how fuel pin internal pressure affects the clad/fuel response (with and without hydrides).	Vary pressure over a wide range to see what effects this variable may have given other changes in the clad/fuel condition. *Precursor activity – Update of the FEA model to incorporate NRC experimental data*
7. Conduct FEA of BWR fuel to understand what to expect from the in cell vibration testing (similar analyses as was done on PWR clad/fuel).	Develop an understanding of how BWR clad/fuel will differ from PWR clad/fuel under load and vibration. Determine which BWR clad/fuel variables are most important. *Precursor activity – None*
8. Conduct FEA to determine the appropriate surrogate materials that can best simulate the UNF dynamic response.	Develop out-of-cell simulation of dynamic performance to match that of UNF dynamic performance carried out in hot-cell testing.

HFIR Irradiation

(Preparation of Samples to Support Follow-on In-Cell Testing)

Test Description	Reason for Test
1. Irradiation of PNNL supplied pre-hydrided test samples (with hydride rim). a. This will support in-cell tests of various different clads to identical conditions (PNNL will supply 4-5 different clads) b. Irradiate some ORNL pre-hydrided samples *[After irradiation, this material will be used for the following tests:* • *CIRFT vibration testing – testing using no surrogate fuel and with surrogate fuel* • *Ring compression testing – testing using no surrogate fuel and with surrogate fuel* • *Anneal material then perform CIRFT testing to evaluate the change in mechanical properties* • *Weld on end caps and pressurize surrogate fueled rodlets;* o *PIE to see if (and how much) the hydrides reoriented* • *Conduct CIRFT tests on the pressurized rodlets*	Simulate LWR high burnup damage. Allow characterization and determination of changes to mechanical properties of cladding with focus on the effects of radiation damage and annealing and how the hydride (and hydride rim) affects clad/fuel strength. a. Compare hydrogen concentrations to ANL high burnup samples *Precursor activities – (1) Develop new test capsule design; (2) Determine hydrogen concentration by neutron scattering*
2. Irradiate some non-hydrided cladding to levels equivalent to the pre-hydrided test samples. [This material will be used for comparison testing to the cladding in Test #1 above, so a similar test matrix will be used].	Establish the separate effects concerning the amount of hydrides and radiation damage. Evaluate whether radial hydride contribution to failure can be established. Requires non-hydrided samples from PNNL.

Neutron Determination of Hydrogen in Hydrided Clads

Test Description	Reason for Test
1. Utilize neutron scattering and tomography to nondestructively evaluate hydrogen content of clad samples: a. PNNL hydrided clad (with hydrided rim) b. ORNL hydrided clad (uniformly distributed hydrides, to be treated for hydride reorientation)	Quantitatively determine the hydrogen concentration, and the hydride morphology of the hydrided samples before inserting the samples into the HFIR, so that the hydrided samples for each alloy can be selected based on their hydrogen contents and distributions in both the axial and circumferential directions). PNNL will supply hydrided samples from 4-5 different clads. ORNL will produce standard samples to calibrate H content for neutron study.

Hot-Cell Testing

Test Description	Reason for Test
1. Replicate dynamic tests of HB Robinson fuel (7.5N; 9N; 10.0N; 12.5N;) a. Perform 2-3 hydride reorientation tests under different hoop stress and repeat the tests above [this will involve defueling the ends of several samples, welding on end caps and pressurizing the samples followed by heating the samples to reorient the hydrides].	Testing of H.B. Robinson (HBR) high burnup fuel at various loads provides a better understanding of the S-N curve; this includes "replicate" tests to ensure reproducibility of results. Based on the UFD Gap Analysis report (Section 5.2.3.5), the radial-hydride embrittlement issue will be investigated with hydride-reoriented samples.
2. Conduct testing of other available PWR fuel (2 Static tests; 1 dynamic calibration; 5 dynamic tests with 2 or more repeat tests): a. TMI Low-Sn Zyr-4 b. Surry-2 Zircaloy-4 c. North Anna M5 d. Catawba M5 (MOX) e. Perform hydride reorientation tests for some selected samples	Testing of other PWR alloys – low Sn Zyr-4, M5 provides information on the similarities or differences clad's material properties may have to transportation during NCT. Hydride reorientation testing needs would be based on the results of the tests done to the HB Robinson fuel above.
3. BWR UNF tests a. Limerick BWR-4 (2 Static tests; 1 dynamic calibration; 5 dynamic tests with 2 or more repeat tests) b. Perform 2-3 hydride reorientation tests under different hoop stress and repeat the tests above.	BWR fuel won't have the pellet-clad bonding that high burnup PWR fuel exhibits. These tests will show how it differs in response from PWR fuel.
4. Conduct CIRFT tests on lower burnup commercial fuel (30 – 40 GWd/MT) under the same conditions as the high burnup UNF was tested. 5. Perform 2-3 hydride reorientation tests under different hoop stress conditions.	Establish the differences between cyclic loading failure rates of high burnup and lower burnup fuels. NOTE: it is very likely that the lower burnup samples will be "ductile", but radial hydride might cause them to become brittle.
6. Conduct ring compression tests on commercial fuel samples (fueled) at RT and at elevated temperature.	Ring compression tests (RCT) will be conducted on the samples that will then be compared to existing RCT data with high burnup samples by ANL. This testing will provide information on how much strength the fuel provides to the clad/fuel system.
7. Conduct ring compression tests on PNNL and ORNL pre-hydrided, HFIR irradiated test samples (various clad types) at RT and elevated temperature (no surrogate fuel in samples).	Provide a linkage between data collected using lab pre-hydrided test samples and LWR irradiated test samples.
8. Conduct ring compression tests on PNNL and ORNL pre-hydrided, HFIR irradiated test samples (various clad types) at RT and elevated temperature WITH surrogate fuel.	Ring compression tests (RCT) will be conducted on the samples that will then be compared to existing RCT data with high burnup samples by ANL. This testing will provide information on

Test Description	Reason for Test
	how much strength the fuel provides to the clad/fuel system.
9. Anneal some HBR samples and test to load levels used in previous experiments (non-pressurized tests).	Determine if annealing changes the mechanical properties in such a way as to change the amount of cycles to failure (shifts the S-N curve).
10. Conduct CIRFT tests on HFIR irradiated PNNL/ORNL cladding a. Conduct tests without annealing samples i. Un-hydrided ii. Pre-hydrided b. Anneal some of the clad samples, conduct CIRFT testing i. Un-hydrided ii. Pre-hydrided	After the HFIR irradiation, pellets will be placed in the clad and CIRFT testing will be completed with the goal of determining the separate effects of hydriding and annealing on the clad. Understand the effect of annealing on the cladding samples and compare the results to the data collected from the annealing of the commercial fuel samples.
11. CIRFT test PNNL and ORNL irradiated/pre-hydrided samples (various clad types) that have had the hydrides reoriented, and perform tests under different hoop stresses. a. This testing will require end caps to be welded on the samples, rodlet pressurization, heating and controlled cooling of the test samples prior to testing.	Determine how much the radial hydrides contribute to clad/fuel system strength change.
12. Test high burnup samples to "equivalent" NCT cycles and loads (peak expected cycles and loads) – test the **unbroken** samples (including PIE). a. Conduct tests on PWR fuel b. Conduct tests on BWR fuel	Provide the program with photographic and numeric test results from samples that have undergone NCT (without failure) to demonstrate to the public what the UNF will look like under expected NCT conditions.
13. Perform CIRFT tests of defueled clad (limited number of cladding types – differences between clads should be insignificant).	Separate effects tests to help understand how much of the total system strength comes from the fuel and how much comes from the clad.
14. Test high burnup WE 17×17 to obtain material data values for stiffness, bend failure, and cyclic fatigue failure characteristics.	Data can be directly utilized in current modeling initiatives and are representative of the bulk majority of what will be transported in the future.
15. Test 17×17 specimens with significant hydride reorientation (then compare the 15×15 data to the 17×17 data to have representative material data).	Compare 15×15 UNF with 17×17 UNF to see if there are any differences in material responses to vibration during NCT.

Out-of-Hot-Cell Testing

Test Description	Reason for Test
1. Tests to evaluate pellet/clad features. a. Fuel chamfer effects (modern pellet chamfer vs. older, non-chamfered pellets b. More/less bambooing of cladding c. Determine effects of significant creep down vs less creep down d. Conduct tests to understand pellet to pellet interface issues (understand existing mechanical properties)	Support modeling efforts by getting a better understanding of: • Fuel clad fracture mechanics. • Hydride and hydride reorientation effects • Effect of gaps in the UNF system • Interface bonding efficiency • Spent fuel-fuel dynamic coupling effects • develop unirradiated vibration properties to determine equipment/testing variability and uncertainties.
2. Pressurize some unirradiated samples (pre-hydrided) to evaluate the effect of clad internal pressure induced by HBU fission gas release to UNF fatigue strength.	Support the in-cell testing of fuel clad pressurization effects.
3. Conduct CIRFT tests to understand fuel and spacer grid interaction effects	Investigate the pinching and fretting effects at the grid spacer during NCT.
4. Test to evaluate hydrogen level and morphology (i.e. distribution and orientation) effects. Hydride reorientation tests should be performed at different temperatures and hoop stresses and hydride orientation. a) Ring compression tests (surrogate fueled) b) Fatigue dynamic tests	Understand the effects of hydrogen content and morphology, including hydride rim and radial hydrides. These are benchmark tests and will provide baseline data for in-cell tests. The ring compression results can be correlated and compared to existing ANL data with defueled high burnup sample.
5. CIRFT testing to understand the possible effects of annealing on UNF during transportation	Evaluate the effect that vacuum drying has on the UNF. This addresses the gap Annealing of Radiation Damage.
6. Conduct mechanical tests on cladding from PNNL. a. Test “as received” cladding	Establish mechanical properties so that future comparisons with post-HFIR irradiated materials will be valid.
7. Conduct tests with simulated clad/fuel samples to verify the FEA on equipment dynamic performance and to estimate correction factors to cope with system dynamic inertia and system resistance.	Understand the energy dissipation from the CIRFT system inertia, system friction, and system alignment related resistance under dynamic vibration. Determine any effects from these issues on the effective load transfer from the CIRFT to the test sample.
8. Conduct tests on simulated clad/fuel samples with similar properties of UNF system to see if out of cell tests can get the same (or similar) results as achieved on irradiated samples in hot cell tests.	The goal is to develop a program that can use extensive out of cell tests while using limited hot cell testing as a validation of the out of cell tests.

Testing of Non-Irradiated and Irradiated Samples (PIE)

Test Description	Reason for Test
1. Conduct SEM on samples of the "as received" PNNL clad samples.	Document the starting condition of the PNNL supplied cladding. Establish microstructural characterizations of the cladding before irradiation.
2. Examine MET mounts and SEM from samples of HFIR irradiated clad	Determine the changes caused by irradiation. Determine the "starting condition" of the cladding prior to hot cell testing.
3. Examine MET mounts and conduct SEM of circumferential and radial hydrided clad samples (PNNL/ORNL) after irradiation.	Establish the condition of the hydrided cladding after irradiation/pressurization/heating to see how much the hydrides reoriented.
4. Conduct SEM on failure surfaces of "broken" NRC/UFD samples to understand the failure mechanisms and locations. a. Evaluate hydrides (etching) b. Determine the process of sample failure c. Examine the fracture surface (Microscopy) d. Examine pre-fracture features (Microscopy) e. Characterize pre-test pellet-pellet interface	Determine the role hydrides (both radial and circumferential) had in the failure. Find out if there were precursors to failure that can be seen before failure; examine the pellet-to-pellet interface failure to understand its importance. Understand why the rods breakwhere they do (are there already pre-existing flaws in those locations; is it the pellet to pellet ridging that is causing the crack initiation.

This page intentionally left blank.